Synaptic phosphoproteome modifications and cortical circuit dysfunction are linked to the early-stage progression of alpha-synuclein aggregation.

Sayan Dutta[1,7], Jennifer Hensel*[1,7], Alicia Scott*[1,7], Rodrigo Mohallem[2], Leigh-Ana M Rossitto[3], Hammad Furqan Khan[4,7], Teshawn Johnson[1], Christina R Ferreira[5], Jackeline F. Marmolejo[2,8], Xu Chen[3], Krishna Jayant[4,7], Uma K. Aryal[2,8], Laura Volpicelli-Daley[6], Jean-Christophe Rochet**[1,7]

*Contributed equally

**Correspondence and requests for materials should be addressed to Jean-Christophe Rochet: jrochet@purdue.edu

[1]Borch Department of Medicinal Chemistry and Molecular Pharmacology, Purdue University, West Lafayette, IN, 47907, USA

[2]Department of Comparative Pathobiology, College of Veterinary Medicine, Purdue University, West Lafayette, Indiana, 47907, USA

[3]Department of Neurosciences, School of Medicine, University of California, San Diego, 92161, USA.

[4]Weldon School of Biomedical Engineering, West Lafayette, Indiana, 47907, USA

[5]Metabolite Profiling Facility, Bindley Bioscience Center, Purdue University, West Lafayette, IN 47907

[6]Center for Neurodegeneration and Experimental Therapeutics, University of Alabama at Birmingham, Birmingham, AL 35294, USA

[7]Purdue Institute for Integrative Neuroscience, Purdue University, West Lafayette, IN, 47907, USA

[8]Purdue Proteomics Facility, Bindley Bioscience Center, Purdue University, West Lafayette, Indiana, 47906, USA

Abstract

Cortical dysfunction is increasingly recognized as a major contributor to the non-motor symptoms associated with Parkinson's disease (PD) and other synucleinopathies. Although functional alterations in cortical circuits have been observed in preclinical PD models, the underlying molecular mechanisms are unclear. To bridge this knowledge gap, we investigated tissue-level changes in the cortices of rats and mice treated with alpha-synuclein (aSyn) seeds using a multi-omics approach. Our study revealed significant phosphoproteomic changes, but not global proteomic or lipid profiling changes, in the rat sensorimotor cortex 3 months after intra-striatal injection with aSyn preformed fibrils (PFFs). Gene ontology analysis of the phosphoproteomic data indicated that PFF administration impacted pathways related to synaptic transmission and cytoskeletal organization. Similar phosphoproteomic perturbations were observed in the sensorimotor cortex of mice injected intrastriatally or intracortically with aSyn PFFs. Functional analyses demonstrated increased neuronal firing rates and enhanced spike-spike coherence in the sensorimotor cortices of PFF-treated mice, indicating seed-dependent cortical circuit dysfunction. Bioinformatic analysis of the altered phosphosites suggested the involvement of several kinases, including casein kinase-2 (CK2), which has been previously implicated in PD pathology. Collectively, these findings highlight the importance of phosphorylation-mediated signaling pathways in the cortical response to aSyn pathology spread in PD and related synucleinopathies, setting the stage for developing new therapeutic strategies.

Introduction

Parkinson's disease (PD) is a neurodegenerative disorder involving a complex array of motor and nonmotor symptoms (1, 2). A key pathological feature of PD is the death of dopaminergic neurons that project from the substantia nigra pars compacta (SNpc) to the striatum, which is largely responsible for the disease's motor symptoms (3). PD neuropathology is also characterized by the presence in multiple brain areas of intracellular Lewy pathology enriched with fibrillar forms of the presynaptic protein, α-synuclein (aSyn)(4, 5). Lewy pathology is found in the brains of individuals with PD as well as other neurodegenerative diseases associated with pathological aSyn aggregation, such as dementia with Lewy bodies (DLB) (5) and multiple system atrophy (MSA) (6), collectively known as synucleinopathies. Although the motor symptoms of PD can be managed successfully for several years with current treatments, the effectiveness of these medications diminishes over time, and there are no effective treatments for non-motor symptoms, nor any available therapies to slow the progression of the disease (7).

Post-mortem analyses of PD brains at various stages of the disease indicate that aSyn aggregates initially appear in the olfactory bulb and brainstem and progressively spread to the midbrain and cortex as the disease advances(8, 9). Additionally, the injection of preformed fibrils (PFFs) of recombinant aSyn in rodent striatum leads to a spread of Lewy-like pathology through anatomically connected neuronal pathways(10, 11, 12). aSyn pathology propagation in both synucleinopathy patients and PFF-injected rodents is believed to involve the release of aggregates from affected neurons into the extracellular space. The secreted aggregates are then taken up by neighboring healthy neurons, where they promote the aggregation of endogenous cytosolic aSyn via a seeding mechanism(13). aSyn aggregates secreted into the CSF can be detected as a readout of underlying aSyn pathology in patients' brains patients using seed amplification assays(14).

aSyn is involved in the regulation of synaptic vesicle release and membrane dynamics as part of its normal physiological function (15, 16). Conversely, aSyn aggregates are known to have various pathogenic effects, including mitochondrial impairment and the dysregulation of proteostasis and lipid homeostasis(17, 18, 19, 20). In primary cultures with seeded alpha-synuclein fibrils, early formation of aggregates leads to impaired connectivity(21). Both primary culture and ex vivo slice electrophysiology studies show alpha-synuclein aggregates impair synaptic transmission(22, 23) . Accordingly, intracellular seeded aSyn propagation is predicted to lead to various forms of cellular dysfunction in rodent PFF models, involving either a loss of aSyn normal function as the monomeric protein is recruited into growing aggregates (24), or a gain of toxic function due to the accumulation of the aggregates themselves(25). However, information is lacking regarding the functional perturbations associated with aSyn pathology propagation in the brains of PFF-injected rodents, especially during the early stages of aggregate spread that occur well before the onset of neurodegeneration.

In this study, we characterized the proteome, phosphoproteome, and the lipid profiling in cortical homogenates from rats three months after intrastriatal injection with either aSyn PFFs or control aSyn monomer. This timeframe allowed for the formation of Lewy-like aggregates in PFF-treated animals without resulting in overt neurodegeneration or behavioral deficits. Phosphoproteomic analysis revealed pronounced PFF-dependent changes, leading to the identification of multiple phosphoprotein hits involved in cellular transport and synaptic function. These phosphoproteomic perturbations were validated in a mouse aSyn PFF model, which exhibited corresponding PFF-dependent changes in neurocircuitry function. Many of the phosphoprotein targets up-regulated in the brains of PFF-treated rats or mice were predicted substrates of casein kinase-2 (CK2). Collectively, these results provide insights into cellular perturbations that could accompany the spread of cortical aSyn pathology in the brains of individuals with PD and other synucleinopathy disorders.

Results

PFF-induced aSyn aggregation leads to phosphoproteomic (but not global proteomic) changes in rat sensorimotor cortex.

To identify molecular perturbations associated with the propagation of aSyn pathology, rats were injected unilaterally in the striatum with aSyn preformed fibrils (PFFs) or monomer (Figures 1A, B) using established methods(10). Brain samples were collected 3 months post-injection and processed for histology or proteomic, phosphoproteomic, or lipid profiling. Immunohistochemical analysis revealed that aSyn PFFs (but not the control monomer, Supplementary Figure 1A) induced the formation of aggregates that stained positive for pS129-aSyn in various brain regions, including the sensorimotor cortex (Figure 1C; Supplementary Figure 1B). Aggregates were found to be distributed among all cortical layers, especially layers IV and V, based on an analysis of sections stained for N-terminal EF-hand calcium-binding protein 1 (NECAB1), a neuronal protein specifically expressed in cortical layers IV/V (Figure 1C).

Analysis of cortical homogenates via liquid chromatography-mass spectrometry (LC/MS-MS) led to the identification of 31,772 unique peptides (label-free quantitation (LFQ) > 0 in at least one sample) derived from 2,799 unique proteins. Following rigorous selection criteria (intensity observed in >70% of the samples in at least one of the two treatment groups), 2,159 proteins met this stringent cutoff, with only 116 proteins exhibiting a raw p-value below the cutoff value for significance (<0.05; Figure 1D) and having a q-value below 0.5. Unsupervised 2D principal component analysis (PCA) revealed two independent overlapping clusters (Figure 1E), confirming that there were no pronounced global proteomic changes attributable to cortical aSyn aggregation at the 3-month time point. Next, we conducted similar analyses of other PD-relevant brain regions including the amygdala (AMG) and substantia nigra (SN) (Supplementary Figure 1, C-I). Consistent with our findings from studies of the sensorimotor cortex, no significant proteomic differences were observed in these regions when comparing the PFF- and monomer-injected animals.

Based on evidence that aSyn pathology can alter kinase localization or activity(26, 27), we next examined phosphoproteomic changes in sensorimotor cortex samples from rats injected with aSyn PFFs or monomers. Changes in the phosphorylation states of synaptic proteins have been implicated as key cellular mechanisms in the dynamic regulation of neuronal synapses, even in the absence of altered protein expression levels(28, 29, 30). We detected 3565 unique phosphopeptides (LFQ>1) from 1509 distinct proteins. After data filtering, 2473 phosphosites with distinct multiplicities, mapping to 1058 proteins, were detected. Of these phosphosites, 220 (i.e., 8.9%, corresponding to 154 unique proteins) exhibited significant changes in abundance (q-value<0.1) in the brains of PFF-treated rats compared to animals injected with aSyn monomer (Figure 1G). Unsupervised PCA revealed two distinct clusters, providing evidence of differences in the phosphoproteome profile between these groups (Figure 1H). These findings suggest that cell signaling perturbations resulting in altered phosphorylation events play a role in synaptic dysfunction induced by seeded aSyn aggregation.

Finally, given the well-documented interaction of aSyn (in both monomeric and aggregate form) with cellular membranes (15, 16, 19, 20), as well as evidence of changes in lipid homeostasis in the brains of PD patients (31), we conducted the profiling of 11 lipid classes on cortical homogenates from aSyn PFF- and monomer-treated rats. However, the analysis of these lipids did not reveal any significant differences or noteworthy fold changes in lipid composition between the two groups (Figure 1F). Similar lipidomic analyses were performed on the AMG and SN, yielding comparable results with no significant differences (data not shown).

Gene ontology analysis reveals alterations in cellular processes involved in synaptic transmission in the brains of PFF-injected rats.

Among the 220 significantly up-or down-regulated phosphosites (i.e., with q<0.1), a 2-fold increase or decrease in intensity was observed in 172 and 9 phosphosites, (respectively) in cortical homogenates prepared from rats injected with aSyn PFFs versus monomer (Figure 2, A-B). A cluster heatmap of log2-transformed intensities for the 50 lowest q-value phosphosites further highlights distinct patterns of up- and-down-regulated phosphoproteins in samples obtained from PFF- versus monomer-treated animals (Figure 2, C). Only a subset of phosphosites within individual phosphoproteins exhibited PFF-dependent dysregulation, suggesting that seeded aSyn aggregation alters site-specific phosphorylation rather than overall protein expression in the rat PFF model. This conclusion is also supported by the absence of any significant changes of the parent peptide in the global proteomics dataset.

Genes associated with significantly up- and down-regulated phosphosites were further examined via gene ontology (GO) enrichment analysis. 'Synaptic organization' emerged as the most enriched term, involving >25 genes encoding pre- and post-synaptic scaffolding proteins (e.g., Piccolo, Bassoon, Rims1, Shank1, Shank3), proteins involved in modulating synaptic vesicle pools and neurotransmitter release (e.g., Dmxl2, Sv2A), and proteins linked to the generation of action potentials (e.g., Grin2a, Grin2b). Top biological processes included terms such as 'vesicle-mediated transport at synapse', 'modulation of chemical synaptic transmission,' and 'synaptic vesicle localization', suggesting that the observed phosphoproteomic changes reflected alterations in synaptic function associated with PFF-mediated aSyn aggregation. Examination of enriched cellular localization terms revealed 'post-synapse' (39 genes) and 'pre-synapse' (32 genes) as the two most enriched terms, with minimal overlap. Pathways related to cytoskeletal organization were also identified from our analysis of enriched 'cellular localization' and 'molecular functions' terms. Moreover, many phosphosites exhibiting changes in abundance in the brains of PFF-treated rats were derived from or associated with protein kinases, suggesting that PFF administration induced changes in kinase activity. Notably, the largest cluster within the 'molecular functions' category revealed by a GO enrichment analysis of genes encoding significantly up- or down-regulated phosphosites included 25 ontology terms related to 'protein kinase binding' (Figure 2, D). Kinases identified by examining our list of up- or down-regulated phosphosites for any peptides mapped to a kinase included members of the CaMK and MAPK families, as well as the AMPK complex.

Western blot analysis of selected synaptic and cytoskeletal proteins confirmed that the observed phosphoproteomic changes did not reflect major alterations in protein abundance, consistent with the global proteomics results (Supplementary Figure 2). Nevertheless, we reanalyzed the global proteomic dataset using a relaxed statistical approach, where proteins with p<0.05 (despite a q-value > 0.1) were subjected to KEGG pathway analysis. The results revealed 'Parkinson's disease' as the most significantly enriched pathway, with 3 of 8 proteins within the pathway consisting of 20S proteasomal subunits (Supplementary Figure 3A). However, biochemical assays did not show significant differences in proteasomal activity between cortical lysates from PFF- versus monomer-injected animals (Supplementary Figure 3B), consistent with the non-significant fold changes observed with the proteasomal hits (q>0.1).

PFF-induced phosphoproteomic changes observed in the rat sensorimotor cortex are also evident in a mouse synucleinopathy model.

To independently validate the PFF-mediated phosphoproteomic changes observed in the rat sensorimotor cortex, we repeated the experiment using a mouse aSyn PFF model. C57BL/6 mice were unilaterally injected with aSyn PFFs (a new preparation relative to the one used for the rat study) or control monomer, either in the striatum or directly in the sensorimotor cortex. After a

3-month incubation period, homogenates were prepared from the sensorimotor cortex of mice in all four groups and processed for phosphoproteomic analysis (Figure 3, A-B). We identified approximately 3,500 phosphosites, with a larger proportion showing a trend towards up-regulation compared to down-regulation in cortical homogenates of mice injected with PFFs in the striatum or cortex (Figure 3, C-D; Supplementary Figure 4, A-B). A total of 526 and 296 sites exhibited significant changes in abundance (q-value<0.1) in the brains of mice injected with PFFs versus monomer in the striatum or cortex, respectively. As observed in the phosphoproteomic dataset derived from analyses of rat cortex, only a subset of phosphosites within individual phosphoproteins exhibited PFF-dependent dysregulation. PCA (Figure 3, E-F) and heatmap analysis (Supplementary Figure 4, C-D) revealed a clear separation between the PFF- and monomer-treated groups, independent of the injection site, providing strong evidence of differences in the phosphoproteome profiles between PFF- and monomer-injected animals. Moreover, the phosphosite hits observed in the brains of mice injected with aSyn PFFs in the striatum or cortex were highly correlated (supporting figure 5, A), further suggesting that the observed changes are due to seeded aSyn aggregation, irrespective of the site of inoculation. These findings underscore the robustness of the observed differences and suggest that seeded aSyn aggregation induces altered phosphorylation events associated with cell signaling perturbations in the mouse sensorimotor cortex.

PFF-induced aSyn aggregation leads to synaptic dysfunction and neurocircuitry perturbations in the mouse sensorimotor cortex.

Genes associated with significantly up- and down-regulated phosphosites in cortical homogenates of PFF-treated mice (independent of injection site) were further investigated via GO enrichment analysis. Examination of enriched cellular localization terms revealed categories related to synaptic function (e.g., ‘post-synapse’, ‘pre-synapse’, ‘axon’, ‘dendrite’), cytoskeletal organization (e.g., ‘structural constituent of cytoskeleton’), and protein kinase binding (Figure 4A). Several phosphopeptides were found to originate from the CaMK, MAPK, and AMPK families (as observed in the rat phosphoproteomics dataset), as well as the PKA family. Additionally, GO analysis of dysregulated phosphosites derived from CAMK2G, PRKAB, PRKAR, and the MAPK kinase family in our phosphoproteomic dataset revealed 'post-NMDA receptor activation events' as the primary disrupted pathway. Similar results were obtained when the GO analysis was performed on genes associated with significantly up- and down-regulated phosphosites in cortical homogenates of mice injected in either the striatum or cortex (Supplementary Figure 5, B-C).

Based on these findings, we measured circuit activity as a proxy for synaptic dysfunction in the sensorimotor cortex of mice treated with aSyn PFFs or monomer. To assess whether seeded aSyn aggregation induces changes in cortical activity, we carried out silicon probe recordings in mouse primary motor cortex 3 months after aSyn PFF injection (Figure 4B). Quantification of spiking activity across the recording session revealed sparser firing of putative layer 2/3 (L2/3) pyramidal neurons compared to layer 5 (L5) neurons (Figure 4C). In addition, we observed notable differences in firing activity across distinct layers in relation to the PFF injection site (Figure 4, D-E). In mice injected in the striatum, L5 (but not L2/3) pyramidal neurons showed an increase in average spiking rates (Figure 4D). In contrast, both L2/3 and L5 pyramidal neurons exhibited increased spiking rates in animals receiving intracortical injections (Figure 4E). Given that striatal aSyn PFF injection leads to pathology predominantly in layer 4/5, whereas PFF injection directly into the cortex induces extensive pathology across additional layers including L2/3 (Figure 3A, B), these data suggest that the observed layer-specific differences in firing rates between intrastriatally versus intracortically injected mice reflect the different patterns of aSyn propagation induced dysfunction across the two sets of animals. Moreover, we infer that the precise location of aSyn seeding is a key determinant of the extent of hyperexcitability induced

within the primary motor cortex. Neuronal hyperexcitability was also observed in the cortex of GCaMP6 mice over a period of 2 to 3 months after intrastriatal or intracortical PFF injection, as demonstrated through live calcium imaging (Khan et al, 2024).

Next, we examined whether the observed increase in spiking activity among individual neurons in the cortex of PFF-treated mice was intricately interconnected within a network. To address this question, we computed the coherence between the spikes of any given pair of neurons within L2/3 and L5 (Supporting figure 6A), yielding a frequency-resolved measure of spike coupling across these pairs. The spike-spike coherence was markedly increased across frequencies of 5 to 20 Hz in mouse cortex 3 months after intrastriatal or intracortical injection with aSyn PFFs versus control monomer (Supplementary Figure 6B). Taken together, these data suggest that PFF injection leads to a dynamic network transition, characterized by increased fluctuations across slow (200 ms) to intermediate (50 ms) timescales, signifying enhanced correlation within the cortical neuronal population. Thus, aSyn pathology has a complex impact on translaminar cortical activity, affecting both firing rates and network connectivity. These changes in neurocircuitry function correlate with, and could potentially be a consequence of, the perturbations of synaptic activity suggested by the phosphoproteomic data.

Because our GO analysis revealed enriched cellular localization terms related to cytoskeletal organization (Figure 4A), we analyzed the spine density of cortical neurites in the brains of mice injected with aSyn PFFs or monomer. Our rationale for these measurements was based on two factors: (i) cytoskeletal destabilization is closely related to a loss of neurite integrity (32), and (ii) a decrease in dendritic spine density was previously observed in mouse cortex 5 months after intrastriatal aSyn PFF injection(33). Contrary to these earlier findings, we observed no significant differences in spine density between mice injected with aSyn PFFs or monomer, regardless of the injection site (Supplementary Figure 7). This result indicates that a decrease in spine density does not occur in our mouse aSyn PFF model at the 3-month timepoint, despite evidence of phosphoproteomic perturbations leading to altered cytoskeletal organization in the brains of these animals.

PFF-mediated phosphoproteomic changes are predicted to involve alterations in the activity of several kinases.

To gain insight into the nature of the kinases – and, therefore, the potential signaling pathways – involved in aSyn PFF-mediated phosphoproteomic alterations, we examined phosphosites that were significantly up- or down-regulated in the brains of PFF-treated rats or mice for evidence of phosphorylation motif enrichment. The analysis was carried out separately for the sequence window of phosphosites showing significant increases or decreases in phosphorylation, as determined by comparing data obtained for PFF- versus monomer-treated animals within each cohort (striatally-injected rats, striatally-injected mice, and cortically-injected mice). The results are shown in Figure 5A, where the frequency of individual amino acids at each position in the phosphorylation site is represented by relative size in a sequence logo. Most of the identified phosphorylation sites contained a serine or threonine residue, suggesting that PFF-mediated changes in serine/threonine kinase activity contribute to the observed phosphoproteomic changes. Many of the motifs that were up- or down-regulated in the brains of PFF-treated animals showed an enrichment of amino acids with negatively charged side chains, such as aspartate (D) or glutamate (E). This finding implies that acidophilic kinases, which have a high propensity to bind acidic residues in their target substrates through electrostatic interactions, exhibit altered activities in the brains of PFF-injected rats or mice. Additionally, we noted the presence of SpP and TpP motifs with high motif scores (i.e., high levels of enrichment). However, because such motifs tend to be overrepresented in enrichment studies, they were not considered further.

Next, we performed kinase predictions on the up- or down-regulated phosphosites within each cohort by comparing them to known consensus motifs targeted by specific kinases. Motifs that were found to be enriched in our datasets are shown in a bar graph (Figure 5B), with each bar manually annotated with the corresponding predicted kinases based on their prediction scores. Among the down-regulated phosphosites in the brains of rats or mice injected with aSyn PFFs in the striatum, the motif xSpPxxxKSx was significantly enriched. This sequence is predicted to be a common substrate for CDK5, GSK3, and p38 MAPK, suggesting that aSyn pathology leads to a decrease in the activity of these kinases. Conversely, the up-regulated phosphosites in the brains of PFF-injected rats or mice were enriched with motifs predicted to be casein kinase 2 (CK2) substrates (e.g., SpDxD, SpDxE, and SpDxxxxE, all with motif scores >300). Additionally, we identified the canonical PKA sites RxxSp and RRxSp among the list of up-regulated phosphosites in the brains of mice injected intrastriatally or intracortically with PFFs. These results suggest that aSyn pathology leads to increased activity of CK2 and PKA in rodent brain.

Discussion

The spread of aSyn pathology in the brains of rodents injected intrastriatally with PFFs follows a pattern determined by the anatomical connectivity of different brain regions to the striatum(11). Of relevance to the current study, PFFs injected in the striatum are taken up by corticostriatal neurons via endocytosis in the synaptic region. Once internalized, PFFs are thought to escape from the endocytic compartment and induce the aggregation of cytosolic aSyn, which is abundant at the synaptic terminal of the recipient neurons(34). Aggregates then spread gradually in a retrograde manner from the synapse to the cell body. This spread of aSyn pathology is cell type-specific, with excitatory neurons of layer IV/V (Figure 1C) being particularly susceptible to aggregate formation and propagation(35, 36, 37) , closely mimicking the pathology observed in human PD(38).

Although cortical pathology becomes evident in rodents within 15 days of intrastriatal PFF administration (Khan et al. 2024), motor and cognitive deficits appear much later(12, 36, 39). This slow disease progression and the modest initial behavioral phenotype closely mirror the early stages of synucleinopathy diseases such as PDD and DLB(40). Accordingly, this model is well-suited for investigating early cortical cellular events that precede overt neurodegeneration. To this end, we carried out proteomic, phosphoproteomic, and lipid profiling analyses of brain homogenates from rats and mice injected intrastriatally or intracortically with aSyn PFFs, 3 months post-injection. Unexpectedly, the global proteomic analyses revealed only a small number of proteins with significant changes in abundance in the brains of PFF-injected animals across various brain regions, based on p-values but not on q-values from FDR-corrected significance tests (Figure 1, D-E, Supplementary Figure 1). Comparing our results with data from one previous global proteomic analysis(41) of aSyn PFF-injected mice revealed substantial overlap between our list of dysregulated proteins and those identified in the earlier studies. However, our analysis did not reveal significant differences in the levels of these proteins between PFF- and monomer-injected animals, likely due to the study's limited power relative to the variability of the global proteomics data or perhaps global expression changes become more pronounced at longer times post-injection. This issue with statistical power and also impossibility of looking at more lipids classes such as cerebrosides, gangliosides and epilipids(42) due to the limited sample amount may also explain the lack of significantly dysregulated lipids revealed by our lipid profiling analysis of brain homogenates (Figure 1F).

In contrast to the low hit rate observed in our global proteomic study, phosphoproteomic analysis led to the identification of 220 phosphosites from 166 proteins that were differentially regulated in cortical homogenates of PFF- versus monomer-injected rats, with most being up-regulated ≥ 2-fold. Similar results were obtained with mice injected with aSyn PFFs in the striatum

or cortex (Figure 3, Supplementary Figure 4). Among the differentially phosphorylated proteins observed in PFF-treated rats or mice were pre- and post-synaptic scaffolding proteins, proteins involved in synaptic vesicle pool regulation and release, and proteins involved in postsynaptic signaling. GO analysis of the proteins associated with the top differentially regulated phosphosites further validated disruptions of cellular processes critical for synaptic function (e.g., chemical synaptic transmission, axon guidance, dendritic formation, microtubule transport) in the brains of PFF- versus monomer-injected animals(Figure 2D, Figure 4A). Changes in cellular pathways involved in synaptic function have also been observed in recent global transcriptomics analysis of brain samples from aSyn PFF-injected mice and PD patients (37, 43, 44). However, in contrast to these studies, we failed to observe changes in total synaptic protein expression levels in rats, as described above (Supplementary Figure 3). This discrepancy may reflect a divergence between mRNA and protein expression changes, as reported by others(45, 46).

Previous studies have demonstrated significant perturbations of the synaptic phosphoproteome during acute synaptic depolarization (29, 30). In this study, we show that chronic protein aggregation similarly disrupts the phosphorylation states of synaptic proteins. Notably, there was minimal overlap between the phosphosites altered in our study and those referred to above, and the serine phosphorylation sites identified here were not significantly enriched for the RxxS motif, a known CaMKII target during Ca^{2+} influx (29, 30). Together, these results suggest that the phosphoproteomic changes observed in the brains of PFF-treated rats or mice are likely driven by chronic, PFF-induced signaling disruptions rather than acute Ca^{2+} influx. These findings are consistent with previous reports of aberrant synaptic connectivity in brain samples from PD or DLB patients, as well as in rodent synucleinopathy models, where the degree of synaptic dysregulation is associated with aggregate burden (22, 23, 43). aSyn is known to localize to the synaptic terminal, where it interacts with other synaptic proteins and plays a significant role in synaptic vesicle homeostasis (34, 47, 48) . We propose that the recruitment of monomeric aSyn into aggregates displaces it from its normal synaptic localization, leading to altered synaptic protein distribution, disrupted activity, and changes in synaptic phosphorylation, ultimately impairing synaptic function and causing circuit irregularities. Similar to the results presented here, phosphoproteomic analysis of cortical samples from AD patients at various stages of disease revealed changes in cellular pathways related to synaptic function (49). This finding suggests that dysregulation of synaptic phosphoproteins in the cortex may be a common molecular feature underlying cognitive deficits associated with neurodegenerative disorders such as PD and AD.

Additional differentially regulated phosphopeptides in the brains of PFF-treated rats or mice were derived from proteins with molecular functions related to cytoskeletal homeostasis, including ‘tubulin binding’ and ‘microtubule binding’ (Figure 2D, Figure 4A). Among the most highly phosphorylated proteins in this category were Map1a, Map1b, and Map2, key components of pre- and post-synaptic terminals(37). PFF-mediated perturbations of these and other cytoskeletal proteins could account for previously reported decreases in axonal transport in primary neuronal culture models treated with aSyn PFFs (21). Moreover, these perturbations could potentially contribute to decreases in spine density observed in the brains of PFF-injected mice during later disease stages (e.g., 5 months after injection), as reported by Herms and colleagues(33), although spine density remained unaffected in our early-stage model (Supporting Figure 7).

The dysregulation of synaptic and cytoskeletal phosphoproteins in PFF-injected rodents suggested that neurocircuitry function might be altered in the brains of these animals. In support of this idea, we observed lower spike rates and altered spike coherence in the sensorimotor cortex of mice injected with aSyn PFFs, either intrastriatally or intracortically (Figure 4, D-E). Conversely, additional studies by our group (Khan H. et al., 2024) revealed that changes in neurocircuitry function appear as early as 4 weeks after PFF injection. Specifically, we observed Tthese changes are characterized by increases in the amplitude of ‘beta events’ (spontaneous bursts of beta transients) driven by NMDA receptor and voltage-gated Ca^{2+} channels (VGCC) signaling. Our

phosphoproteomic data provide a molecular basis for these neurocircuitry disruptions, implicating dysregulation of NMDA receptor-related phosphoproteins such as Grin2a/2b, Shank3, and the Dlg family in PFF-injected mice (e.g., figure S10, S11 in Khan H., et al., 2024), along with up-regulation of VGCC subunits Cacna1b and Cacnb1 in PFF-injected rats (this study). Future studies will aim to determine whether the observed phosphoproteomic changes affecting synaptic proteins, cytoskeletal components, NMDA receptors, or VGCCs contribute directly to the neurocircuitry alterations evident in the brains of PFF-injected mice.

Protein kinases contributing to phosphoproteomic alterations in the brains of PFF-injected rats or mice were identified by examining our list of up- or down-regulated phosphopeptides for any kinase-derived peptides. In both the rat and mouse datasets, we identified phosphopeptides originating from the CaMK, MAPK, and PKA families, as well as the AMPK complex. In particular, we observed enrichment of MAPK3 (ERK1) peptides phosphorylated on T202 and Y204, as well as MAPK1 (ERK2) peptides phosphorylated on T185 and Y187, in the brains of mice injected with PFFs in the striatum or cortex. These results suggest that both kinases are activated as a result of seeded aSyn aggregation *in vivo*, consistent with previous data showing enhanced MAPK3 and MAPK1 phosphorylation at these sites in the brains of aSyn transgenic mice and DLB patients (50). Evidence that MAPK1 and PRKACA are associated with pS129-aSyn in Lewy bodies (51) implies that interactions between these kinases and pathological aSyn could play a role in altered kinase activity driving the phosphoproteomic changes observed in the brains of PFF-treated rodents. Moreover, our finding that 'post-NMDA receptor activation events' was the primary disrupted pathway from a GO analysis of dysregulated phosphopeptides derived from CAMK2G, PRKAB, PRKAR, and the MAPK kinase family suggests that these kinases could contribute to the PFF-mediated dysregulation of NMDA receptor signaling discussed earlier.

As a second approach to identifying protein kinases involved in PFF-mediated phosphoproteomic changes, we scanned our list of up- or down-regulated phosphosites for enriched consensus motifs targeted by specific kinases (Figure 5). This analysis revealed decreased CDK5, GSK3, and p38 MAPK activities, as well as increased CK2 and PKA activities, in the brains of PFF-injected rats or mice. The PFF-dependent up-regulation of CK2 activity is particularly intriguing given this kinase's suggested role in PD pathogenesis and progression. Specifically, CK2 phosphorylates aSyn on residue S129, a modification thought to influence the protein's toxicity and propensity to aggregate (52). Furthermore, the CK2 regulatory beta subunit, CK2β, has been shown to co-localize with pSer129^{+} aggregates in the substantia nigra(27). As one possible mechanism, CK2β recruitment into aSyn aggregates could result in an increased concentration of free catalytic subunits, CK2α and CK2α', in the synapse, leading to dysregulated (increased) catalytic activity and altered phosphorylation of CK2 targets(53). Alternatively, changes in CK2β phosphorylation at residues S3, S4, and S209, observed in our phosphoproteomic dataset, could contribute to the increased CK2 activity(54, 55) in the brains of PFF-injected rats or mice. Conversely, CK2 is abundantly expressed by glial cells with previous literature describing its increased occurrence in astrocytes in Alzheimer's Disease human post-mortem tissue(56). Given that the tissues analyzed had mixed cell types, glial cells, in particular astrocytes, may also play a role in promoting increased CK2 activity.

In conclusion, our findings suggest that seeded αSyn aggregation induces significant changes in protein phosphorylation, largely driven by increased CK2 activity, in the sensorimotor cortex of rats and mice injected with aSyn PFFs. In turn, these phosphoproteomic changes disrupt key signaling pathways linked to NMDA receptor function, VGCC activity, and cytoskeletal dynamics and are accompanied by neurocircuitry dysfunction. The involvement of additional kinases with altered activity, including PKA, CDK5, GSK3, and p38 MAPK, underscores the complex interplay of signaling pathways contributing to aSyn-mediated neuronal dysfunction. Understanding the molecular mechanisms linking aSyn-induced phosphoproteomic changes to neurocircuitry impairment will be critical for developing therapies to mitigate cognitive decline in PD and other synucleinopathies.

Experimental Methods

Recombinant aSyn protein purification:

Mouse recombinant aSyn was purified as described (57, 58). *E. coli* BL21 (DE3) cells transformed with the bacterial expression vector pT7-7 encoding mouse aSyn were incubated in LB medium supplemented with ampicillin (100 µg/L) at 37°C until the optical density at 600 nm reached 0.5-0.6. Protein expression was induced with isopropyl β-D-1-thiogalactopyranoside at a final concentration of 1 mM, followed by incubation at 37°C for 4 h. The cells were then harvested by centrifugation, resuspended in lysis buffer (10 mM Tris HCl, pH 8.0, 1 mM EDTA, 0.25 mg/mL lysozyme), and lysed using a French press cell disruptor (Thermo Electron, Waltham, MA) at > 1000 psi. The lysate was treated with 0.1% (w/v) streptomycin sulfate to precipitate DNA and then clarified by centrifugation. The supernatant was subjected to partial purification via two successive ammonium sulfate precipitations (30% and 50% saturation) at 4°C. The resulting pellet was resuspended in 10 mM Tris-HCl (pH 7.4), and the suspension was boiled at 95°C for 15 min. Following centrifugation at 13,500 × g at 4°C for 20 min to precipitate denatured proteins, aSyn was purified from the supernatant via successive fractionations using: (i) a HiLoad 16/600 Superdex 200 pg size exclusion column (Cytiva, Marlborough, MA), with elution performed in 10 mM Tris HCl (pH 7.4); and (ii) a HiPrep Q HP 16/10 (Cytiva) or DEAE (GE Healthcare Bio-Sciences) anion exchange column, with elution performed using a linear gradient of 25 mM to 1 M NaCl in a buffer consisting of 10 mM Tris HCl (pH 7.4) and 1 mM EDTA. Fractions enriched with aSyn or aSyn-mVenus (identified via SDS-PAGE with Coomassie blue staining) were pooled, and the solution was dialyzed against PBS (10 mM phosphate buffer, 2.7 mM KCl, and 137 mM NaCl, pH 7.4). aSyn preparations used for preformed fibril (PFF) formation were depleted of endotoxin using the Pierce high-capacity endotoxin removal resin (cat no. 88277, Thermo Fisher Scientific, MA, USA) to 0.018 units/µg of protein (3). The purified protein was stored at -80°C until use, with a final purity of approximately 95%.

Preparation of aSyn PFFs:

A 500 µL solution of monomeric mouse aSyn (5 mg/mL) was filtered through a 0.22 µm filter (Cat. no. 8160, NY, USA) and incubated in a sterile 1.5 mL microcentrifuge tube at 37 °C for 7 days with continuous agitation at 1,000 rpm (123 x g) in a Thermomixer (BT LabSystems BT917). The resulting fibrils were concentrated by centrifuging the fibril suspension at 13,000 x g for 10 min and resuspending the pellet in 250 µL of Dulbecco's phosphate-buffered saline (DPBS; Cytiva). An aliquot of the fibril suspension (5 µL) was incubated with 8 M guanidine hydrochloride at 22°C for 1 h to dissociate the fibrils into monomers. The aSyn concentration was determined via absorbance measurements at 280 nm using a Nanodrop spectrophotometer, with an extinction coefficient of 7450 M^{-1} cm^{-1}. aSyn fibrils were stored at −80°C as 25 µL of aliquots at a concentration of 5 mg/mL. Prior to use, aliquots were thawed and sonicated in ethanol-sterilized sonicating tubes (cat. no. 53071, Active Motif, CA, USA) using a cup horn sonicator (cat. no. q700, Qsonica, CT, USA) at 30% power (~100 W/s) with a cycle of 3 s on and 2 s off, for a total 'on' time of 15 min, while maintaining the bath temperature between 5 and 15.**Transmission electron microscopy**:

Recombinant aSyn fibrils were analyzed by negative stain transmission electron microscopy (TEM) as described previously (59). Briefly, 3 µL of fibril suspension (≤ 0.5 mg/mL) was applied to a glow-discharged, carbon-coated copper TEM grid (Electron Microscopy Sciences, CF400CU) and incubated at 22°C for 45 s. The grid was rinsed with deionized water,

followed by the application of 3.5 µL of 1% (w/v) phosphotungstic acid (PTA) as a contrast agent. After a 1-minute incubation, excess PTA was removed by blotting with Whatman filter paper, and the grids were air-dried. Imaging was performed using an FEI Tecnai T12 Transmission Electron Microscope (Thermo Fisher Scientific) operating at 80 kV. Gatan DigitalMicrograph software (Gatan Microscopy Suite) was used to capture the images.

Intracranial PFF injections:

All methods for working with animals were conducted using protocols approved by the Purdue Animal Care and Use Committee (PACUC). In one set of experiments, 3- to 4-month-old male Sprague Dawley rats (Envigo, IN, USA) were secured in a stereotaxic frame (Kopf Instruments, CA, USA) and anesthetized with isoflurane. A suspension of sonicated aSyn PFFs or a solution of control, monomeric protein (4 µL, 5 mg/mL) was injected into the striatum (coordinates: ± 3.5 mm lateral, 0 mm posterior to bregma; 4.5 mm ventral from dura) at a constant flow rate of 0.5 µL/min using a 10 µL Hamilton syringe (Hamilton, NV, USA) fitted with a 30-gauge needle with a 45° angled tip. The needle was left in place for 5 min post-infusion to prevent backflow. In a second set of experiments, 3- to -4-month-old male C57BL/6 J mice (cat. no. 000664, The Jackson Laboratory) underwent stereotaxic injections of aSyn PFFs or monomer (5 mg/mL) into either the primary motor cortex (1 µL delivered at ± 1.8 mm lateral, 0.3 mm anterior to bregma; 0.7 mm ventral from dura) or the striatum (1.5 µL delivered at ± 2 mm lateral, 1 mm posterior to bregma; 2.5 mm ventral from dura). Injections were performed using a 10 µL syringe fitted with a 33-gauge needle at a flow rate of 50 to 100 nL/min. Post-surgical care included administration of ketoprofen (5 mg/kg in normal saline) to rats and 5 mg/kg carprofen plus 6 mg/kg dexamethasone to mice, immediately after surgery and 48 h later.

Brain tissue processing:

Rats or mice were euthanized by an overdose with sodium pentobarbital (50.9 mg/mL) and transcardially perfused with cold PBS. Animals designated for immunohistochemical (IHC) analysis were additionally perfused with 4% (w/v) paraformaldehyde (PFA) in PBS. Brains were quickly removed after decapitation, post-fixed overnight in the same PFA solution, and cryoprotected in 30% (w/v) sucrose in water at 4°C. Coronal sections (40 µm thick) were prepared using a frozen sliding microtome (Thermo Scientific Microm HM430). Sections were stored at -20°C in cryoprotectant solution (30% w/v sucrose and 30% v/v ethylene glycol in 0.1 M phosphate buffer) until IHC analysis. For animals designated for proteomic and lipid profiling, specific brain regions (sensorimotor cortex, amygdala, and substantia nigra) were isolated immediately after perfusing with cold PBS, flash-frozen in liquid nitrogen, and stored at -80°C until further analysis.

Immunohistochemistry:

Free-floating sections were washed 3 times for 10 min each in PBS to remove residual cryoprotectant solution and then incubated in PBS containing Triton X-100 (1% v/v) for 60 min. The sections were blocked in a solution of 10% (v/v) normal donkey serum in PBS supplemented with Triton X-100 (0.3% v/v) (PBST) for 90 min and then incubated with primary antibody solution prepared in PBST containing 1% (v/v) normal donkey serum overnight at 4°C. After washing in PBS (3 x 10 min), the sections were incubated with Alexa fluorophore-conjugated secondary antibodies (Jackson ImmunoResearch Laboratories, 1:500 dilution) at 22°C for 90 min. After a final round of three 10-min washes in PBS, the tissues were mounted on slides, allowed to dry overnight, and sealed with coverslips using DPX mounting media (cat. no. 13512, Electron Microscopy Sciences). The primary antibodies used in these experiments included antibodies

specific for tyrosine hydroxylase (cat. no. AB1542, Millipore Sigma, 1:1000), NECAB1 (cat. no. PA5-54849, Thermo Fisher Scientific, 1:500), and pSer129-aSyn (EP1536Y [cat. no. ab51253, Abcam, 1:500] and 81a [cat. no. MABN826, Millipore Sigma, 1:500])**.**

Sample preparation for proteomic/phosphoproteomic and lipid profiling analyses:

Brain tissue samples (~15-20 mg) were resuspended in 300 µL of 25 mM ammonium bicarbonate (ABC) supplemented with protease and phosphatase inhibitors and homogenized in a Precellys Evolution tissue homogenizer using soft-tissue homogenizer CK14 tubes (Bertin Technologies SAS, France). The total protein concentration was then measured using the bicinchoninic acid (BCA) assay (Thermo Fisher Scientific, MA, USA). The Bligh and Dyer (B & D) extraction method (60) was then performed using lysate volumes equivalent to 25 µg of total protein. The chloroform layer was then carefully transferred to a new tube, dried in a vacuum centrifuge, and used for lipid analysis. Four volumes of cold (-20°C) methanol were then added to the water-methanol layer, and samples were centrifuged at 17,200 x g for 10 min. The supernatant was removed, and pelleted proteins were dried in a vacuum centrifuge. For the phosphoproteomics experiment, tissue lysate containing 500 µg of total protein was precipitated with acetone overnight. The protein pellets (for proteomics and phosphoproteomics experiments) were then resuspended in 10 µL of 8 M urea solution supplemented with 10 mM DTT and incubated at 37°C for 1 h. Next, 10 µL of alkylation reagent mixture (97.5% v/v acetonitrile (ACN), 0.5% v/v triethyl phosphine, 2% v/v iodoethanol) was added, and samples were incubated at 37°C for 1 h. After alkylation, samples were dried in a vacuum centrifuge and subsequently resuspended in 80 µL of 0.025 µg/µL trypsin (Thermo Fisher Scientific). The digestion was carried out using a barocycler (50°C, 60 cycles; 50 s at 20 kpsi and 10 s at 14.7 psi). Peptides were then desalted with a C18 silica MicroSpin column (The Nest Group Inc, USA). For phosphoproteomic analysis, phosphopeptides were enriched with PolyMac spin tips (Tymora Analytical, IN, USA), following the manufacturer's recommendations.

LC-MS/MS analysis:

Peptides were separated using the UltiMate 3000 RSLC nano HPLC system (Thermo Fisher Scientific) connected to a Q-Exactive Orbitrap HF mass spectrometer (Thermo Fisher Scientific) for rat samples, or an Orbitrap Fusion Lumos mass spectrometer (Thermo Fisher Scientific) for mouse samples. The samples were first loaded onto a PepMap trap column (50 mm x 300 mm ID, 5 µm particle size, 100 Å pore size; ThermoFisher Scientific) at a flow rate of 5 µL/min for 5 min using buffer A (0.1% formic acid in water) as the mobile phase. Subsequently, peptides were eluted through an Acclaim PepMap C18 silica column (500 mm x 75 µm ID, 2 µm particle size, 100 Å pore size; ThermoFisher Scientific) at a flow rate of 150 nL/min over a 160-min gradient of buffer A and buffer B (0.1% formic acid in 80% acetonitrile). The gradient was programmed as follows: (i) 2% buffer B to 27% buffer B over the first 110 min, (ii) 27% buffer B to 40% buffer B over the next 15 min, (iii) 40% buffer B to 100% buffer B over 10 min, (iv) constant at 100% buffer B for an additional 10 min, and (v) reset to 2% buffer B.

MS analysis of the mouse samples was performed with the orbitrap detector, with an MS1 resolution of 60,000 and MS2 resolution of 15,000. Quadrupole isolation was set to "True". The scan range was set to 375–1600 m/z. The Radio Frequency (RF) lenses were set to 30%, and the Automatic Gain Control (AGC) target was set to "Standard," with a maximum injection time "Auto", and 1 microscan. A dynamic exclusion duration of the 60 s was used, with the exclusion of isotopes. Data was collected using Data- Dependent Acquisition (DDA) mode with cycle time of 3 s, between scans. The precursor ion (MS1) intensity threshold was set to 5.0×10^3 and peptides were fragmented using high energy collisional dissociation (HCD) with 30% collision

energy. MS/MS data were also collected using “Orbitrap” as a detector, with AGC target “Standard”, maximum injection time “Auto” and 1 microscan and isolation window of 1.2 m/z. The procedures listed above is consistent across previously published works(61, 62, 63).

Lipid analysis:

Brain lipids were analyzed using MRM profiling methods described previously(64, 65). Dried lipid extracts prepared as described above were diluted in injection solvent (300 mM acetonitrile/methanol/ammonium acetate, 3:6.65:0.35 v/v) to obtain a stock solution. This solution was further diluted into injection solvent spiked with 0.1 ng/µL of EquiSPLASH LIPIDOMIX isotopically labeled lipids (cat. no. 330731, Avanti Polar Lipids, AL, USA) for sample injection. MS data were acquired using flow-injection (i.e., without chromatographic separation) of 8 µL of the diluted lipid stock solution delivered using a micro-autosampler (G1377A) to the ESI source of an Agilent 6410 triple quadrupole mass spectrometer (Agilent Technologies, CA, USA). A capillary pump was connected to the autosampler and operated at a flow rate of 7 µL/min and a pressure of 100 bar. The Agilent 6410 was set to acquire lists of multiple reaction monitoring scans (MRMs) related to lipids. The dwell time for each MRM was 40 ms. The MRMs used were based on the Lipid Maps Standard Database (LMSD) for phosphatidylcholine (PC), phosphatidylethanolamine (PE), phosphatidylinositol (PI), phosphatidylglycerol (PG), phosphatidylserine (PS), ceramides, cholesteryl esters, free fatty acids (just single ion monitoring - SIM), triacylglycerols (TG) and diacylglycerols (DG). The MRMs related to PC, PE, PG and ceramides were based on protonated parent ions and class-diagnostic product ions. The MRMs related to PS, PI, DG, TG and CE were based on ammonium adducts for the parent ions, class-diagnostic product ions for the PS, PI and CE lipids, and on fatty acyl neutral losses for the TG and DG lipids. Free fatty acids were detected as deprotonated ions in the negative ion mode. The collision energies and fragmentor and cell acceleration voltage settings were determined based on product ion scan experiments using EquiSPLASH LIPIDOMIX isotopically labeled lipids. The electrospray ionization (ESI) source parameters were gas temperature 300°C, gas flow 5.1 L/min, nebulizer 17 psi, and capillary voltage 4 kV for the positive ion mode and 3.5 kV for the negative ion mode.

Bioinformatics analysis:

Raw LC-MS/MS data were processed using the analysis platforms Maxquant (version 2.0.3.1) (66) and Perseus (67). The data were searched against the *Rattus norvegicus* or *Mus musculus* sequence on UniProt(68) using trypsin as the proteolytic enzyme, allowing up to 2 missed cleavages. Variable modifications were specified for “methionine oxidation” and, in the case of phosphoproteomic analysis, “STY phosphorylation,” while “carbamidomethylation” was assigned as a fixed modification. Other search parameters and data filtering were as described in previously(69) Raw data files were filtered based on contaminants, and intensity values were log 2-transformed. Protein/peptide entries present in >70% of the samples were selected for downstream analysis. Data imputation was performed for the replacement of missing values and data quality validation. A two-sample t-test was performed (with a permutation-based false discovery rate (FDR) correction) on samples obtained from PFF- versus monomer-injected animals. Peptide sequences exhibiting a greater than twofold increase or decrease in abundance in the brains of animals injected with PFFs versus monomer were subsequently analyzed for gene ontology (GO) enrichment. GO analysis and protein-protein interaction network analysis were performed using the Metascape bioinformatics platform (https://metascape.org) (70). Heatmaps were generated in MATLAB, and sample clustering based on principal component analysis was performed using the web platform MetaboAnalyst (71).

Lipid profiling was performed as described previously (64, 65). The MS data were processed using an in-house script to obtain a list of MRM transitions with their respective sums of absolute ion intensities over the acquisition time. Group-average fold changes were analyzed for 11 lipid classes. To determine the group average, intensities were first filtered using a cutoff of 1.3x blank values. Fold change was plotted using Prism 9. Statistical analysis was performed utilizing MetaboAnalyst 5.0. Data on relative amounts were autoscaled to obtain a normal distribution followed by an analysis of heatmap distributions and t-tests with FDR corrections.

Measurement of proteasomal activity using 7-amino-4-methyl coumarin (AMC) probe:

Proteasomal activity was measured in tissue lysates as described by Maher et al (72). Briefly, flash-frozen tissues were lysed in 150 to 400 µL cold assay buffer (50 mM HEPES, pH 7.4, 10 mM NaCl, 1.5 mM $MgCl_2$, 1 mM EDTA, 250 mM sucrose, 1 mM freshly prepared ATP) using a 1/8-inch probe tip sonicator (Fisher Scientific, FB120 with CL-18 probe) set to 30% power, with a cycle of 1 s on and 1 s off for 30 cycles. Lysates were then centrifuged at 13,000 × g and 4°C for 20 min, and protein concentrations in the supernatant were determined using a BCA protein assay kit. For activity measurements, proteins (15 to 30 µg) were diluted into 100 or 200 µL of assay buffer containing 1 mM DTT and 25 µM AMC probe (Enzo Life Sciences, NY, USA). Proteasomal activity was quantified by monitoring the rate of fluorescence increase at 37°C using a Synergy fluorescence plate reader (BioTek Instruments, VT, USA) with excitation and emission wavelengths set to 360 nm and 480 nm. Control reactions were prepared by supplementing lysates with epoxomicin (cat. no. 324800, Millipore Sigma) at a final concentration of 5 µM to inhibit proteasomal activity.

Western blot analysis

Western blot analysis was performed as described (73). Briefly, frozen brain samples were homogenized in RIPA buffer (50 mM Tris HCl, pH 7.4, 150 mM NaCl, 0.1% (w/v) SDS, 0.5% (w/v) sodium deoxycholate, 1% (v/v) Triton X-100) supplemented with protease inhibitor, and the supernatant obtained after centrifugation at 10,000 x g was mixed with Laemmli buffer (Bio-Rad Laboratories, CA, USA) containing 5% (v/v) β-mercaptoethanol. The samples were boiled at 95°C for 5 min, and the proteins were separated via SDS-PAGE on a 4 to 20% (w/v) polyacrylamide gradient gel (Bio-Rad) and transferred to a 0.4 µm PVDF membrane. After transfer, membranes were blocked in LiCor blocking buffer for 60 min at 22°C and then incubated overnight at 4°C with primary antibodies against synapsin (cat. No. D1265, Cell Signaling Technology, 1:1000), syntaxin (cat. no. Ab188583, Abcam, 1:1000), synaptobrevin (cat. no. 1933-SYB, Antibodies Incorporated, 1:1000), tau (cat. No MAB3420, Millipore Sigma, 1:500), actin (A5441, Sigma-Aldrich, 1:2000), or tubulin (cat. no. 15115, Cell Signaling Technology, 1:1000). After washing in Tris-buffered saline with Tween 20 (0.05% v/v), the membranes were incubated with secondary antibodies conjugated to infrared dyes (LI-COR Biosciences, NV, USA) for 90 min at 22°C. Imaging was performed using a LiCor imaging system (LICORbio, model 3350), and band densities were quantified using the ImageJ software (NIH, MD, USA).

Golgi-Cox staining:

Golgi-Cox staining was performed using the FD Rapid GolgiStain kit (FD Neurotechnologies, MD, United States). Brains were immersed in the impregnation solution and incubated for 24 h, after which they were transferred to fresh solution and stored in the dark at 22°C for 2 weeks. The brains were then placed in Solution C and incubated at 4°C for 2 d. To achieve uniform freezing, the brains were immersed in 2-methylbutane cooled to -78°C using a

dry ice ethanol bath. Coronal sections (80 μm thick) were then prepared using a cryostat and mounted on gelatin-coated microscope slides. The sections were dried for 2 days, rehydrated in Milli-Q water, and treated with the developing solution. They were then dehydrated in an ethanol series (70%, 80%, and 100% v/v), cleared in xylene, and mounted using DPX mounting medium (Electron Microscopy Sciences, PA, USA). Coverslips were applied to preserve the stained sections for analysis.

Image acquisition and dendritic spine analysis:

Five dendrite sections from layer II/III pyramidal neurons in the cortical region of each mouse were identified and imaged using a laser scanning microscope (Zeiss, Germany) equipped with a 60x objective lens. High-resolution images were captured from the basal compartment of each neuron and uploaded to Neurolucida 360 software (MBF Bioscience, VT, USA). For spine density quantification, a dendritic segment of at least 10 μm in length was randomly selected from from the basal compartment of each of the five neurons per mouse. Each segment was traced, and dendritic spines were manually counted using Neurolucida 360.

Cranial window and electrode implant:

Under sterile conditions, a custom titanium headplate was attached to the skull using vetbond and metabond dental cement. After headplate implantation, mice were allowed to recover in their home cages for 3 d. Mice underwent habituation of head fixation and running on a 6-in rotating wheel for at least one week before electrophysiological experiments were performed. On the day of the experiment, carprofen and dexamethasone were administered subcutaneously. Following previously established methods(61), a small craniotomy (< 1 mm) was made over the primary motor cortex (0.4 mm AP, 1.5 mm ML), and the dura was partially removed. A 64-channel electrode (64D Sharp, Mismanidis Lab) was inserted perpendicular to the surface of the pia using a micromanipulator (Sensapex 4-uMP). The microelectrode was positioned 1 mm into the motor cortex and allowed to settle for 20 min before recordings began. Signals were digitized at a bandwidth of 0.1 to 10 kHz and sampled at 20 kHz (Intan RHD recording system). Probe tracks were confirmed histologically after each experiment to verify electrode placement.

Spike sorting:

After the recording session, the electrical signals were processed to sort action potentials from individual neurons. This sorting was accomplished using Kilosort3, followed by a meticulous manual review in Phy2. Neurons were evaluated based on waveform characteristics, stability of firing rates observed throughout the recording session, and autocorrelograms. To analyze the time-varying response of neurons, peri-stimulus time histograms were generated by creating 2000 ms windows during quiescent mouse activity. Average neural activity traces were smoothed by calculating the mean spiking activity across multiple trials and convolving by a Gaussian filter with a full-width at half-maximum (FWHM) of 10 ms. The depth at which each spike occurred was determined based on the electrode that recorded the maximum waveform amplitude. Spiking analysis was conducted on neurons exhibiting sustained activity throughout the entire recording session. To assess the coherence between two spiking signals, we employed discrete signal taper methods following the approaches described in previous studies (74, 75, 76, 77). The 2000 ms trial period was segmented into multiple 400 ms intervals with a 200 ms overlap, ensuring full coverage. We removed the DC component from each spike train and applied a single Slepian taper, resulting in an effective smoothing of 2.5 Hz for the 400 ms data windows (NW = 1, K = 1). Confidence intervals were determined using jackknife resampling, involving the exclusion of

individual trials. To test whether time-locked trends in firing rate across trials influenced coherence calculations, we performed random shuffles of trial identities and recalculated coherence. This provided a baseline for coherence solely attributed to trends in firing time-locked to the trial. Further, to account for differences in firing rates across neurons within a session, a random number of neurons (5% of the total recorded units) were thrown out, and the coherence was recalculated. This was done a total of 3 times to check for biasing introduced by rate-dependent spiking events. Coherence values were computed based on cross-correlations within trials, followed by cross-correlation pooling across trials and normalization by the power spectra of spike trains, which were also pooled over trials.

Motif enrichment analysis and kinase prediction:

Logos for significantly increased or decreased phosphopeptides in binary comparisons were generated using WebLogo (version 3.7.4) (78). Motif enrichment analysis was done using motifx (R package rmotifx version 1.0) (79). Foreground sequences were sequences of total length 15, +/-7 amino acid residues flanking each phosphosite, that were either significantly increased or decreased in binary comparisons ($p<0.05$, $q<0.1$). Background sequences were extracted from the rat and mouse proteomes (Uniprot UP000002494 and UP000000589, respectively) using helper packages parseDB and extract Background (R package PTMphinder, version 0.1.0) (80). The central residue was set to S, T, or Y, the minimum sequence cut-off was set to 5, and the p-value cut-off was set to 10^{-5}. Enriched motifs are represented by their motif score, which is calculated by taking the sum of the negative log probabilities used to fix each position of the motif. Higher motif scores correspond to more specific and statistically significant motifs. Lastly, kinase prediction was performed using NetPhos3.1 online software, with positive predictions having scores >0.5 (81).

Figure 1

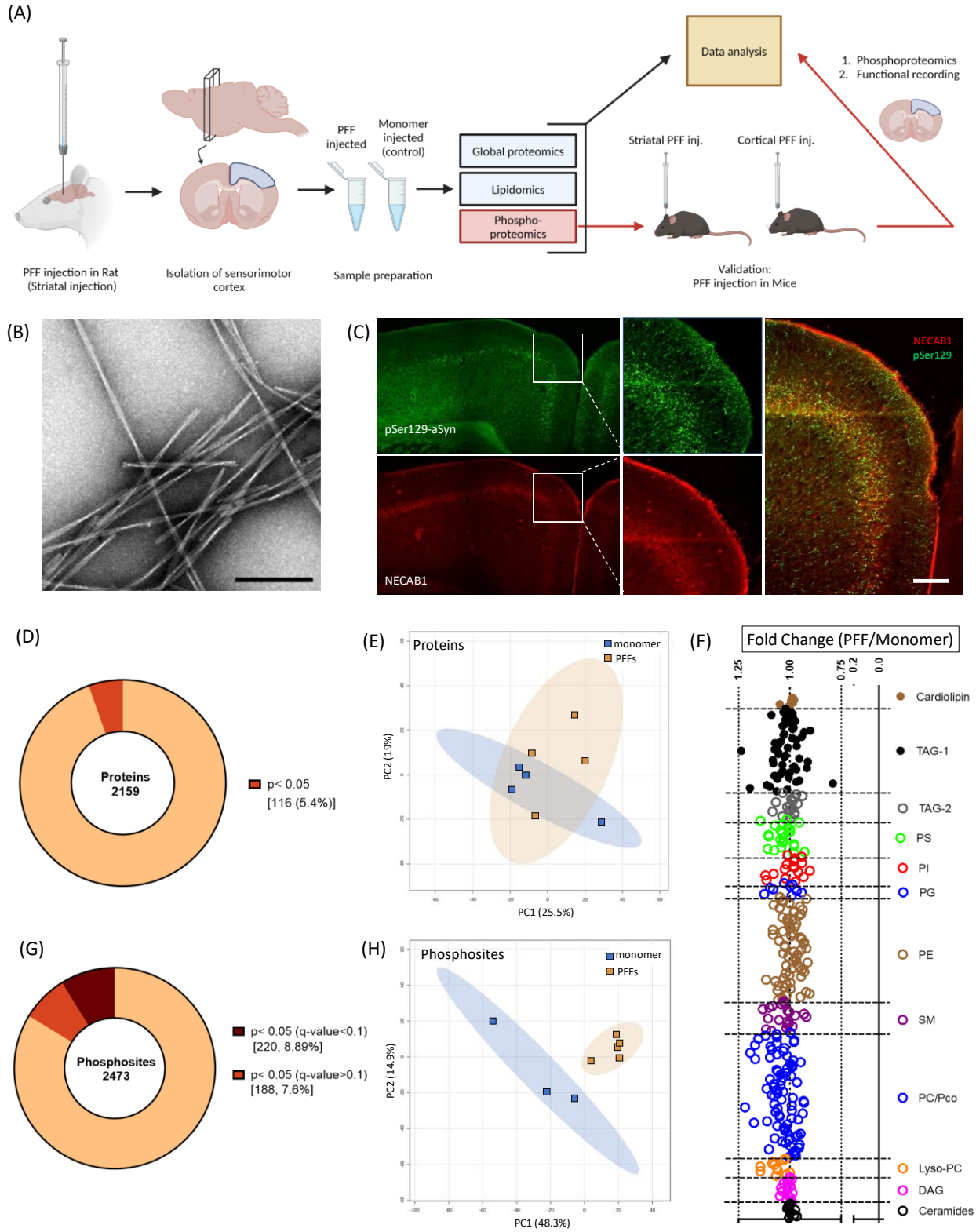
(A)
PFF injection in Rat (Striatal injection)
Isolation of sensorimotor cortex
PFF injected
Monomer injected (control)
Sample preparation
Global proteomics
Lipidomics
Phospho-proteomics
Data analysis
1. Phosphoproteomics
2. Functional recording
Striatal PFF inj.
Cortical PFF inj.
Validation: PFF injection in Mice
(B)
(C)
pSer129-aSyn
NECAB1
NECAB1
pSer129
(D)
Proteins 2159
p< 0.05 [116 (5.4%)]
(E)
Proteins
monomer
PFFs
PC1 (25.5%)
PC2 (19%)
(F)
Fold Change (PFF/Monomer)
1.25
1.00
0.75
0.2
0.0
Cardiolipin
TAG-1
TAG-2
PS
PI
PG
PE
SM
PC/Pco
Lyso-PC
DAG
Ceramides
(G)
Phosphosites 2473
p< 0.05 (q-value<0.1) [220, 8.89%]
p< 0.05 (q-value>0.1) [188, 7.6%]
(H)
Phosphosites
monomer
PFFs
PC1 (48.3%)
PC2 (14.9%)

Figure 1: Rats injected intrastriatally with aSyn PFFs show evidence of phosphoproteomic changes in the sensorimotor cortex.

(A) Overview of the multi-omics approach used to identify cortical changes associated with aSyn aggregation in the rat PFF model (created using https://BioRender.com)
(B) Representative images of aSyn preformed fibrils (PFFs) visualized by transmission electron microscopy. Scale bar: 100 nm.
(C) Representative images of a rat cortical section stained for pS129-aSyn (81a, green) and the cortical layer IV/Layer V-specific marker NECAB1 (red) 3 months after aSyn PFF injection in the striatum (n=3 animals). Scale bar: 200 µm.
(D) Pie chart representation of protein hits obtained via global proteomic analysis of homogenates prepared from rat sensorimotor cortex 3 months after intrastriatal injection with aSyn PFFs or monomer. The chart shows the percentage of hits with $p \geq 0.05$ or $p < 0.05$. Each hit was detected in ≥70% of samples in at least one experimental group.
(E) Graph showing the results of unassigned/unsupervised PCA of the log2-transformed intensities of all protein hits identified in the cortical homogenates described in (d).
(F) Graph showing lipid profiling perturbations (expressed as fold change in lipid level) in the cortical homogenates described in (d). None of the changes were below the significance threshold of $p < 0.05$. TAG, triacylglycerols; PS, phosphatidylserine; PI, phosphatidylinositol; PG, phosphatidylglycerol; PE, phosphatidylethanolamine; SM, sphingomyelin; PC, phosphatidylcholine; DAG, diacylglycerol.
(G) Pie chart representation of unique phosphosite hits obtained via phosphoproteomic analysis of the cortical homogenates described in (D). The chart shows the percentage of hits with $p < 0.05$ ($q < 0.1$) or $p < 0.05$ ($q > 0.1$). Each hit was detected in ≥70% of samples in at least one experimental group.
(H) Graph showing the results of unassigned/unsupervised PCA of the log2-transformed intensities of all phosphosite hits identified in the cortical homogenates described in (G).

Figure 2

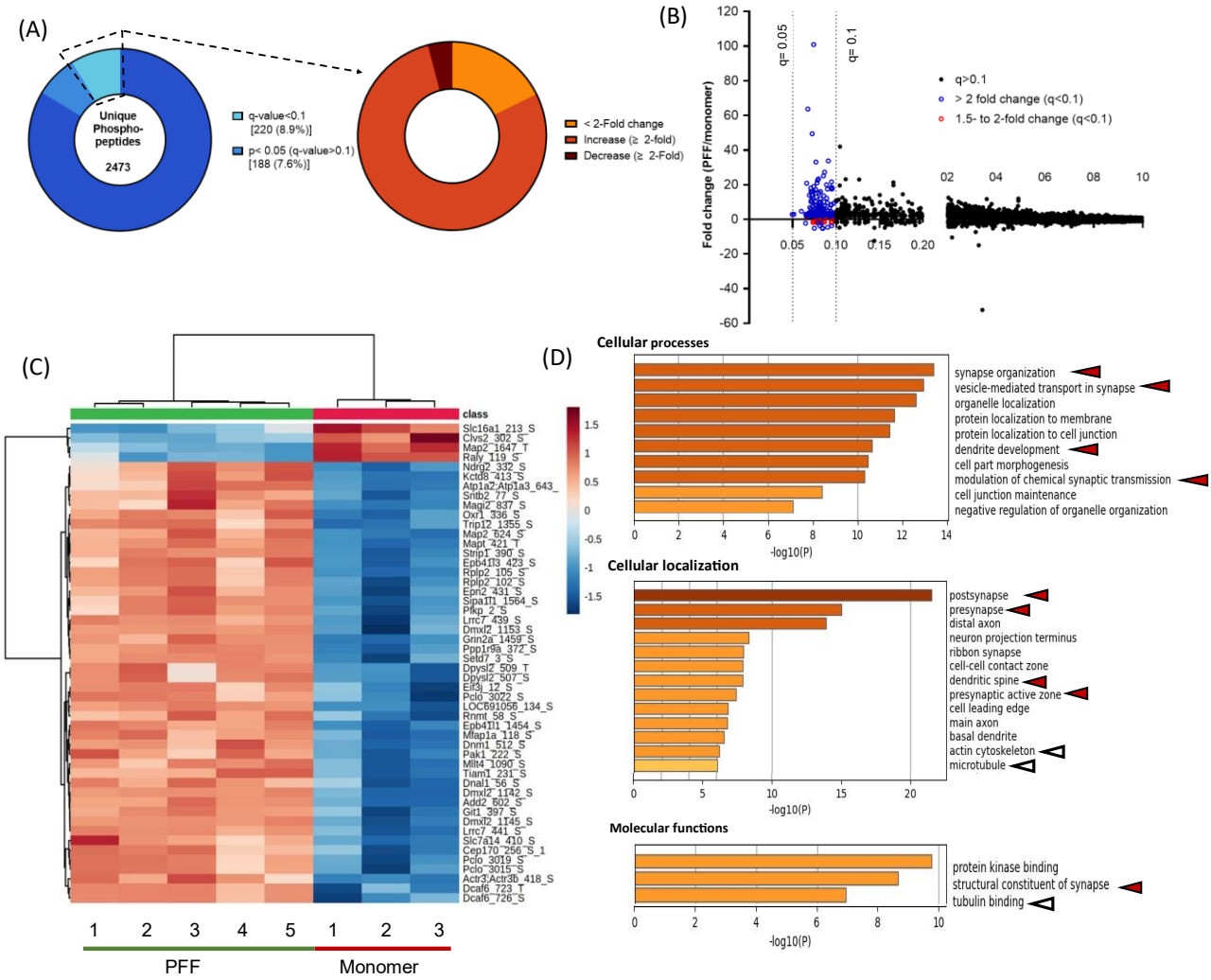
(A)
Unique Phospho-peptides
2473
q-value<0.1 [220 (8.9%)]
p< 0.05 (q-value>0.1) [188 (7.6%)]
< 2-Fold change
Increase (≥ 2-fold)
Decrease (≥ 2-Fold)
(B)
Fold change (PFF/monomer)
q= 0.05
q= 0.1
q>0.1
> 2 fold change (q<0.1)
1.5- to 2-fold change (q<0.1)
(C)
class
PFF
Monomer
(D)
Cellular processes
synapse organization
vesicle-mediated transport in synapse
organelle localization
protein localization to membrane
protein localization to cell junction
dendrite development
cell part morphogenesis
modulation of chemical synaptic transmission
cell junction maintenance
negative regulation of organelle organization
-log10(P)
Cellular localization
postsynapse
presynapse
distal axon
neuron projection terminus
ribbon synapse
cell-cell contact zone
dendritic spine
presynaptic active zone
cell leading edge
main axon
basal dendrite
actin cytoskeleton
microtubule
Molecular functions
protein kinase binding
structural constituent of synapse
tubulin binding

Figure 2: Gene ontology analysis of the top up- or down-regulated phosphoproteins in the sensorimotor cortex of PFF-treated rats reveals perturbations of cellular structures and functions involved in synaptic transmission.

(A) Pie chart representation of phosphosite hits obtained via phosphoproteomic analysis of homogenates prepared from rat sensorimotor cortex 3 months after intrastriatal injection with aSyn PFFs or monomer. The chart shows the percentage of phosphosite hits with q<0.1 that exhibit a fold change of <2 (black) or are up- or down-regulated by a factor of ≥2 (red and blue, respectively). Each hit was detected in ≥70% of samples in at least one experimental group.

(B) Plot showing the phosphosite distribution represented as intensity fold change (PFF/monomer) versus q-value. Phosphosites with q<0.1 that are up- or down-regulated by a factor of 1.5 to 2 or >2 are represented by green and red symbols, respectively. Each phosphosite was detected in ≥70% of samples in at least one experimental group.

(C) Cluster heatmap showing the z-scored log2-transformed intensities of the top 50 up- or down-regulated phsophosites (i.e., phosphosites with the lowest q-values) in the cortical homogenates described in (a). Red and blue colors correspond to an increase or decrease (respectively) in phosphosite levels in rats injected with PFFs versus monomer, and the color intensity represents the Z-score-normalized Log2(intensity) values. Peptide names are listed as 'protein name_phosphoresidue number'.

(D) Charts showing enriched GO terms within cellular processes (top), cellular localization (middle), and molecular functions (bottom) that represent groups of phosphoproteins in the sensorimotor cortex impacted by PFF treatment. GO analysis was carried out on proteins containing phosphosites with q<0.1 and a fold change of ≥2 (see panel A). Arrowheads highlight items relevant to synaptic transmission (red) or the cytoskeleton (white).

Figure 3

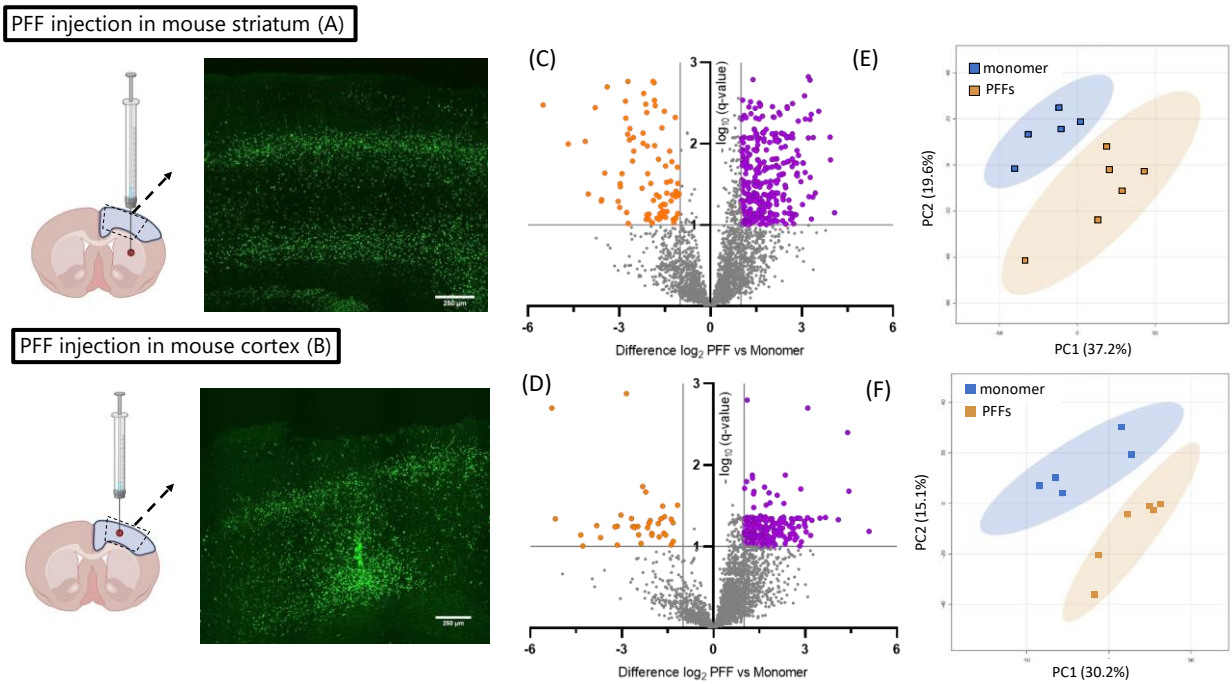

Figure 3: Mice injected in the striatum or cortex with aSyn PFFs show evidence of phosphoproteomic changes in the sensorimotor cortex.

(A, B) Schematics showing the injection site, tissue isolated for phosphoproteomic analysis (blue-shaded region), and approximate cortical section area processed for histology (dashed trapezoid) (LEFT), and corresponding images of pS129-aSyn immunoreactivity (EP1536Y, green) (RIGHT), for mice injected with aSyn PFFs or monomer in the striatum (A) or cortex (B). The sections were prepared 3 months after injection (scale bar: 250 µm) (n=3 animals). (schematic created using https://BioRender.com)

(C, D) Volcano plot distributions of phosphosites found to be up-regulated (orange) or down-regulated (yellow) in homogenates prepared from mouse sensorimotor cortex 3 months after injection with aSyn PFFs versus monomer in the striatum (C) or cortex (D). The plot shows the fold change of the phosphosites in relation to the adjusted p-value (i.e. q-value), where q<0.1 was considered significant, as indicated by the horizontal dashed line.

(E, F) Graphs showing the results of unassigned/unsupervised PCA of the log2-transformed intensities of phosphosite hits in the cortical homogenates described in (C) and (D), obtained from mice injected with aSyn PFFs or monomer in the striatum (E) or cortex (F).

Figure 4

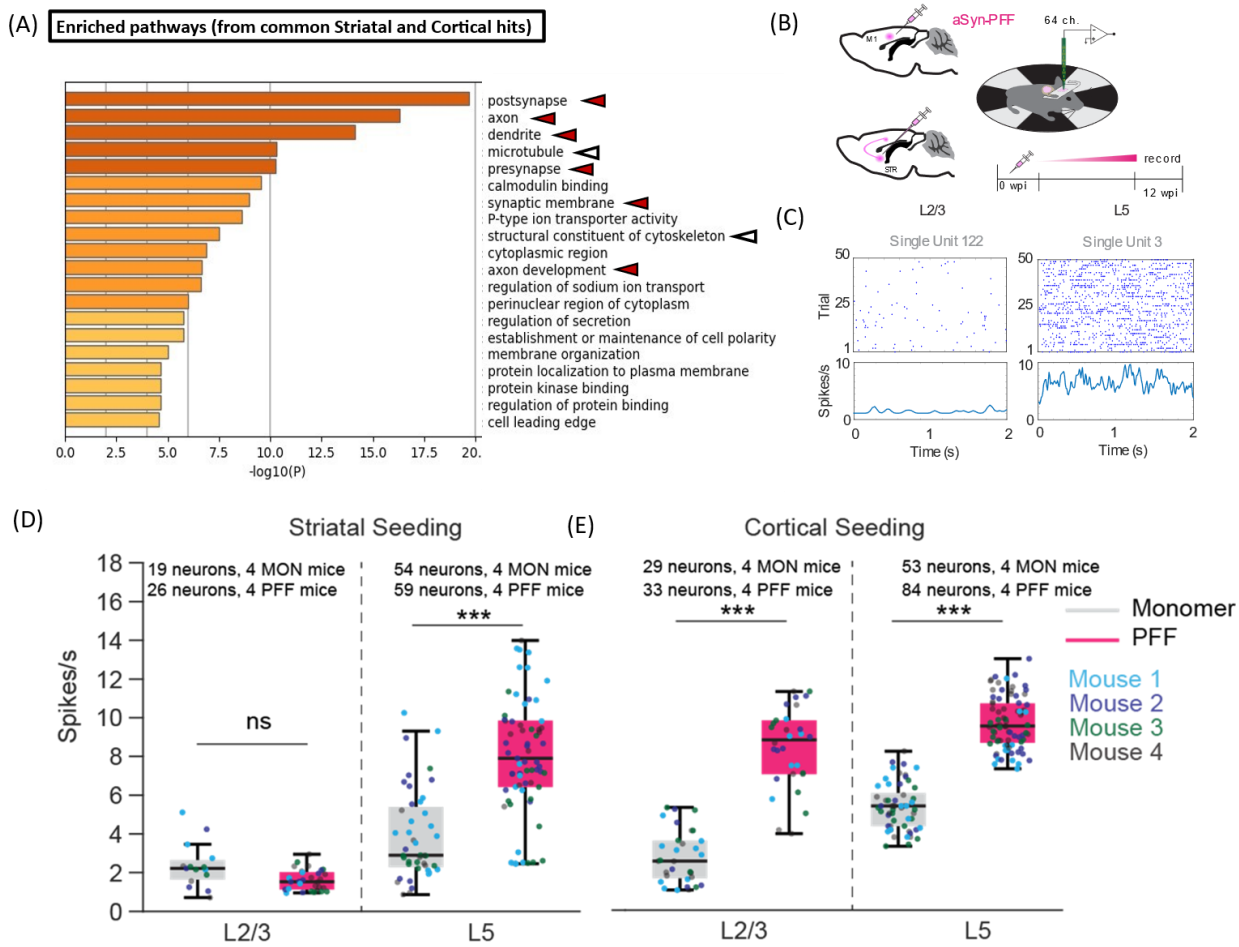
(A)
Enriched pathways (from common Striatal and Cortical hits)
postsynapse
axon
dendrite
microtubule
presynapse
calmodulin binding
synaptic membrane
P-type ion transporter activity
structural constituent of cytoskeleton
cytoplasmic region
axon development
regulation of sodium ion transport
perinuclear region of cytoplasm
regulation of secretion
establishment or maintenance of cell polarity
membrane organization
protein localization to plasma membrane
protein kinase binding
regulation of protein binding
cell leading edge
-log10(P)
(B)
aSyn-PFF
64 ch.
record
0 wpi
12 wpi
L2/3
L5
(C)
Single Unit 122
Single Unit 3
Trial
Spikes/s
Time (s)
(D)
Striatal Seeding
19 neurons, 4 MON mice
26 neurons, 4 PFF mice
54 neurons, 4 MON mice
59 neurons, 4 PFF mice
ns
***
Spikes/s
L2/3
L5
(E)
Cortical Seeding
29 neurons, 4 MON mice
33 neurons, 4 PFF mice
53 neurons, 4 MON mice
84 neurons, 4 PFF mice
Monomer
PFF
Mouse 1
Mouse 2
Mouse 3
Mouse 4

Figure 4: Mice injected with aSyn PFFs show evidence of cortical circuit dysfunction.

(A) Chart showing enriched GO terms in the 'cellular localization' category that represent groups of phosphoproteins in mouse sensorimotor cortex impacted by PFF administration in either the striatum or cortex, 3 months after injection. GO analysis was carried out on proteins containing phosphosites with $q<0.1$ and a fold change of ≥ 2 in at least one group (see Supporting Figure 4A, B). Arrowheads highlight items relevant to synaptic transmission (red) or the cytoskeleton (white).

(B) Schematic illustrating the design of experiments aimed at monitoring neurocircuitry function in mouse sensorimotor cortex. Two separate cohorts of mice were injected with aSyn PFFs or monomer in the primary motor cortex or dorsal striatum. Electrophysiological analyses were carried out at 0 weeks and 3 months (12 weeks) post-injection (0 and 12 wpi).

(C) Example of layer-specific unit activity during awake recording in head-fixed mice injected with aSyn monomer.

D, E) Spiking rates of recorded neurons were analyzed based on cortical depth in mice injected with either aSyn PFFs or monomers into the striatum (D) or cortex (E). Number of neurons recorded per mouse injected in the striatum (D): L2/3 neurons, 3-6 (monomer) and 3-8 (PFF); L5 neurons, 8-15 (monomer) and 10-19 (PFF). Number of neurons recorded per mouse injected in the cortex (E): L2/3 neurons, 5-9 (monomer) and 6-8 (PFF); L5 neurons, 9-16 (monomer) and 11-30 (PFF). Each subgroup includes data from 4 animals. The box plot shows the median and interquartile range (IQR); *** $p<0.0001$, ranked-sum Wilcoxon test.

Figure 5

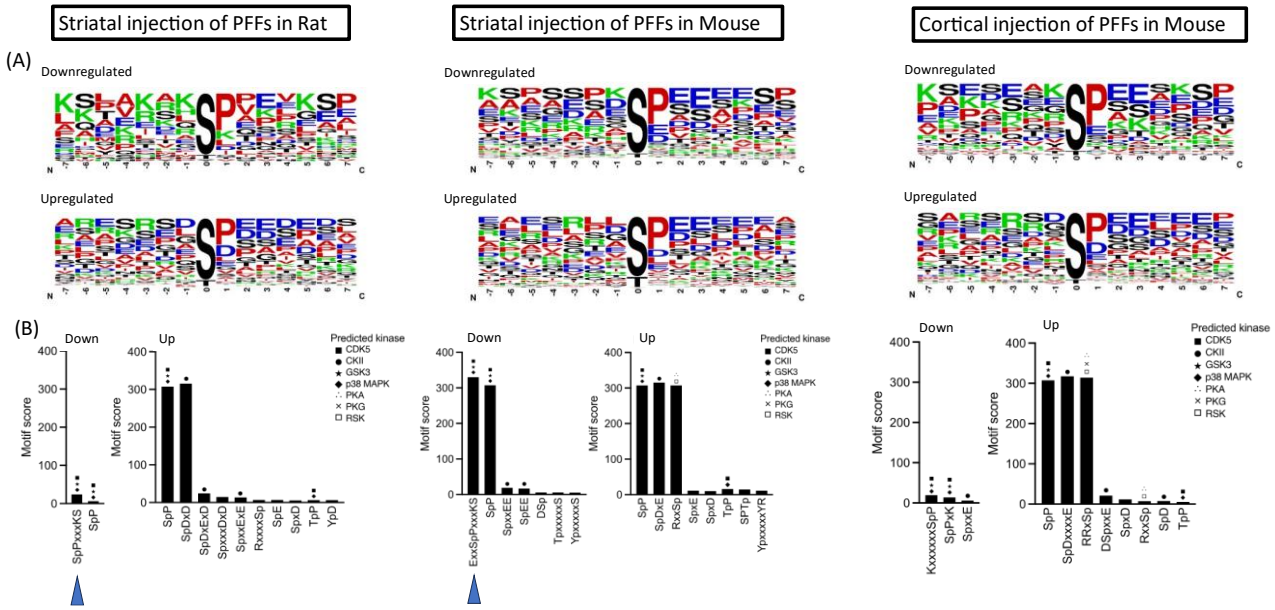

Figure-5: Motif enrichment and kinase prediction analysis implicate altered kinase activity in aSyn PFF-induced phosphoproteomic changes.

A. Sequence logos illustrating the frequency of individual amino acids (with larger size indicating higher frequency) in the sequence window of phosphosite containing peptides that were down-regulated (top) or up-regulated (bottom) in the brains of rats injected with aSyn PFFs in the striatum (left) and mice injected with PFFs in the striatum (middle) or cortex (right). Phosphorylated residue is represented at position 0.

B. Bar graphs depicting enrichment scores for phosphosite motifs identified in significantly down- or up-regulated phosphosites ('down' or 'up') in the brains of rats injected with PFFs in the striatum (left) and mice injected with PFFs in the striatum (middle) or cortex (right). Higher enrichment scores indicate more significant and specific motifs. All displayed motif enrichments and kinase predictions are statistically significant ($p<1 \times 10^{-5}$ or prediction score >0.5, respectively). Symbols for predicted kinases are positioned above each bar in order of their prediction scores, with the highest score indicated by the top symbol.

Supplementary Figure 1

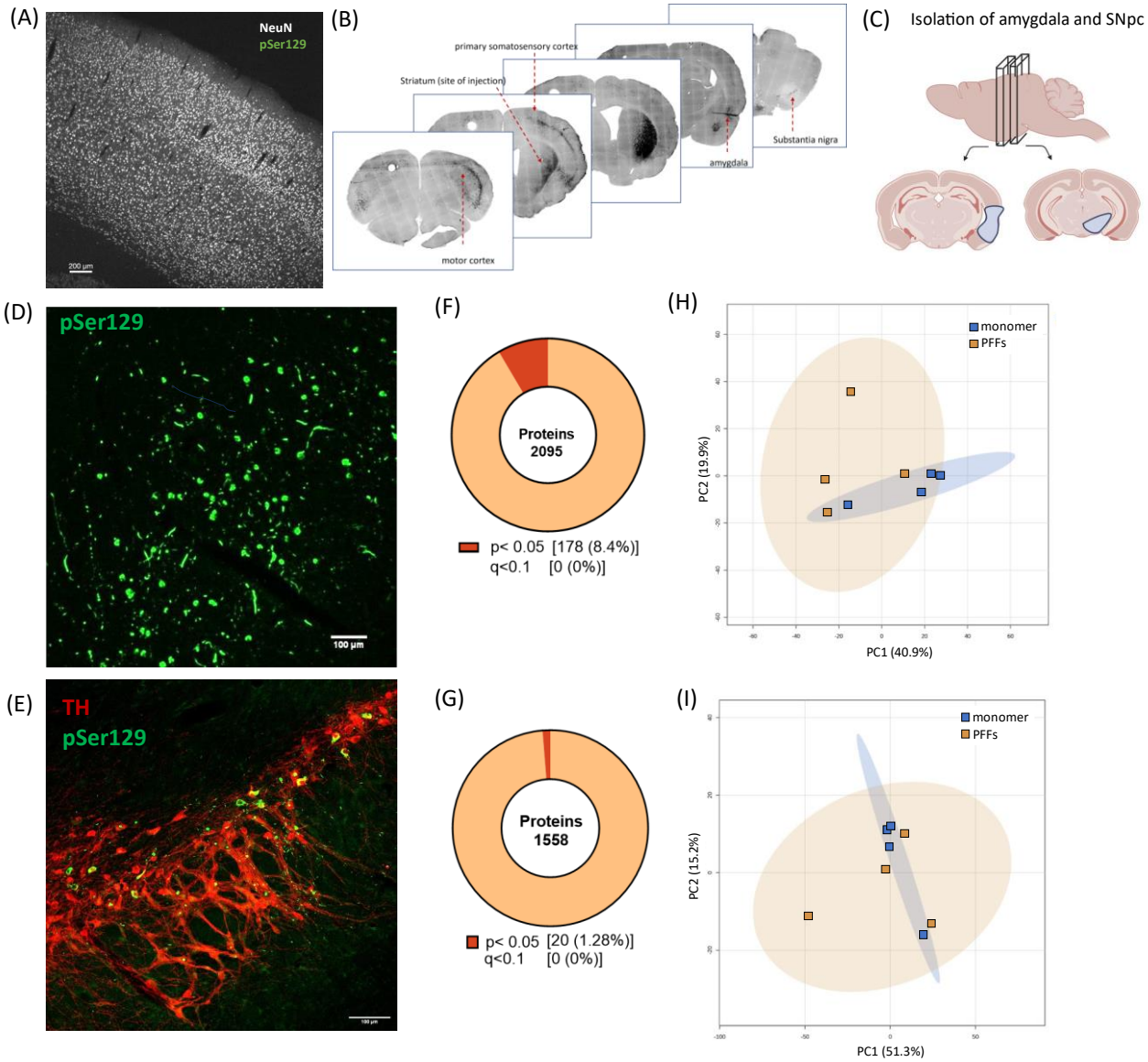

Supplementary Figure 1: Rats injected intrastriatally with aSyn PFFs do not show evidence of pronounced changes in the global proteome in the amygdala or substantia nigra.

(A) Image showing the absence of pS129-aSyn (81a) signal in a rat cortical section stained for the pan-neuronal marker (NeuN, white) 3 months after monomer injection in the striatum. Scale bar: 200 µm.

(B) Representative images of rat brain sections showing pS129-aSyn immunoreactivity in the cortex, striatum, amygdala, and SN 3 months after aSyn PFF injection in the striatum. Serial coronal brain sections were stained with the EP1536Y antibody.

(C) Schematic of serial brain sections used to collect amygdala and SN samples for proteomic analysis. (created using https://BioRender.com)

(D-E) Representative images of rat brain sections showing pS129-aSyn immunoreactivity (EP1536Y, green) in the amygdala (D) or SN (e) 3 months after aSyn PFF injection in the striatum. The nigral section in (E) was co-stained for tyrosine hydroxylase (TH) to demonstrate the presence of pS129-aSyn inclusions in nigral dopaminergic neurons (n=3 animals). Scale bar: 100 µm.

(F-G) Pie chart representations of protein hits obtained via global proteomic analysis of homogenates prepared from rat amygdala (F) or SN (G) 3 months after intrastriatal injection with aSyn PFFs or monomer. The chart shows the percentage of hits with $p<0.05$ or $q<0.1$. Each hit was detected in ≥70% of samples in at least one experimental group.

(H-I) Graphs showing the results of unassigned/unsupervised PCA of the log2-transformed intensities of all protein hits identified in homogenates prepared from rat amygdala (H) or SN (I) as described in (H) and (I).

Supplementary figure 2

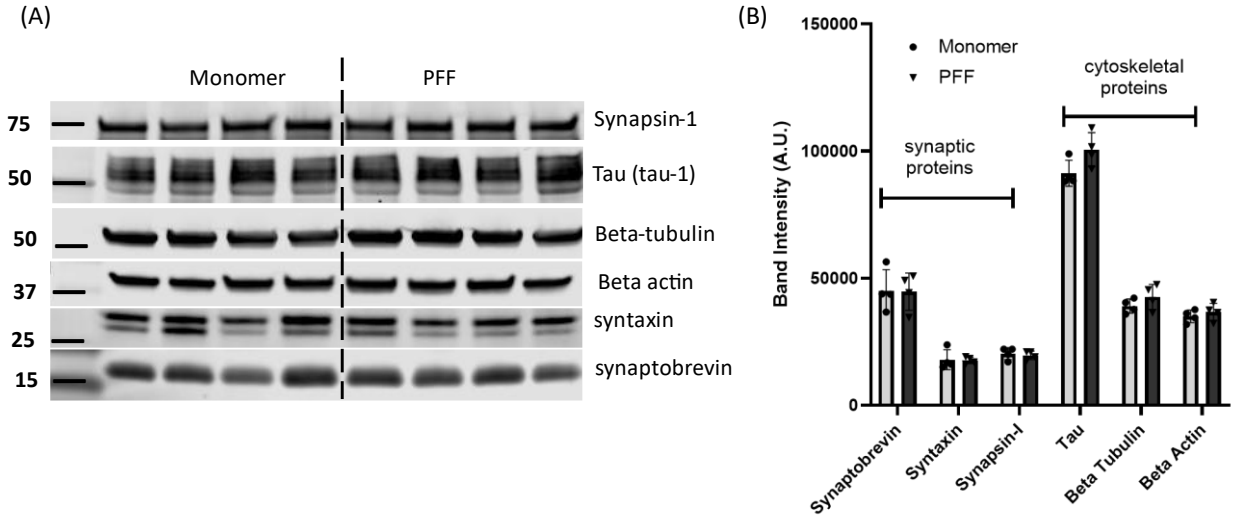

Supplementary figure 2: Exposure to aSyn PFFs does not lead to changes in levels of synaptic or cytoskeletal proteins in rat sensorimotor cortex. (A) Image of Western blot loaded with homogenates prepared from rat sensorimotor cortex 3 months after intrastriatal injection with aSyn PFFs or monomer. The blot was probed with antibodies specific for the synaptic proteins synaptobrevin, syntaxin, and synapsin-1 or the cytoskeletal proteins tau, β-tubulin, and β-actin (n=4 biological replicates). (B) Graph showing band intensities determined for the Western blot in panel A (mean ± SD).

Supplementary figure 3

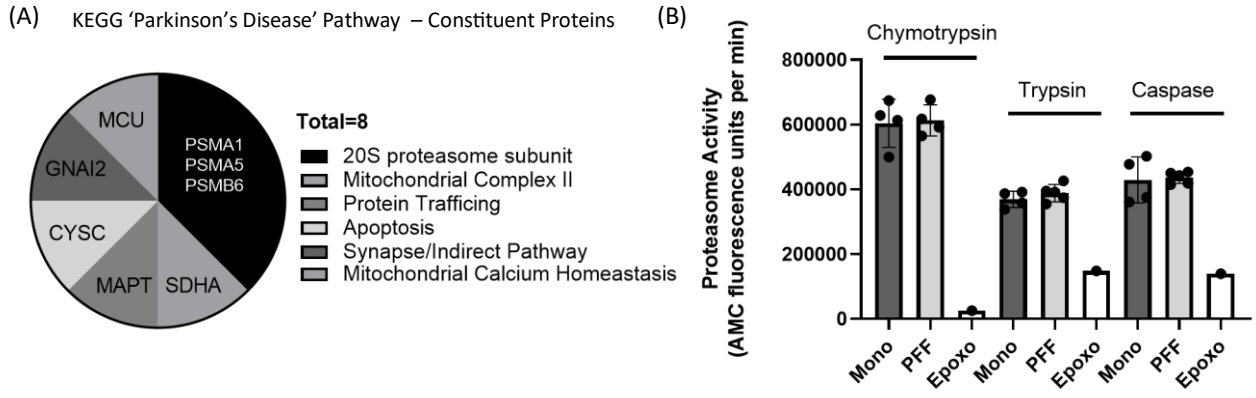

Supplementary figure 3: Exposure to aSyn PFFs may lead to changes in the levels of PD-linked proteins (including 20S proteasome subunits) in rat sensorimotor cortex.

(A) KEGG pathway analysis of proteins from the global proteomics dataset with $p<0.05$ (see Fig. 1D) revealed 'Parkinson's disease' as the most significantly enriched pathway (log p = -5.17, log q = -3.21). The pie chart shows the 8 hit proteins from our dataset that constitute this pathway, classified into subgroups defined by different cellular functions. The largest subgroup ('20S proteasome subunit') contains 3 of the 8 protein hits. PSMA1, proteasome 20S subunit alpha 1; PSMA5, proteasome 20S subunit alpha 5; PSMB6, proteasome 20S subunit beta 6; SDHA, succinate dehydrogenase complex flavoprotein subunit A; MAPT, Microtubule-associated protein tau; CYSC, cystatin C; GNAI2, Guanine nucleotide-binding protein G(i) subunit alpha-2; MCU, mitochondrial calcium uniporter.

(B) Analysis of proteasomal activity in homogenates prepared from rat sensorimotor cortex 3 months after intrastriatal injection with aSyn PFFs or monomer revealed no differences in chymotryptic, tryptic, or caspase-like activity of the 20S proteasome. The graph shows enzyme activities expressed as rates of cleavage of the proteasome substrates SUC-LLVY-AMC (chymotrypsin), Boc-Leu-Arg-Arg-AMC (trypsin), and Ac-Nle-Pro-Nle-Asp-AMC (caspase-like). Bars labeled 'Epoxo' correspond to homogenates prepared from control rats, pretreated with the proteasome inhibitor epoxomicin (n=1; final concentration, 5 μM) for 20 min prior to measuring proteasome activity (mean+/- SD, n=4-5 biological replicates).

Supplementary figure 4

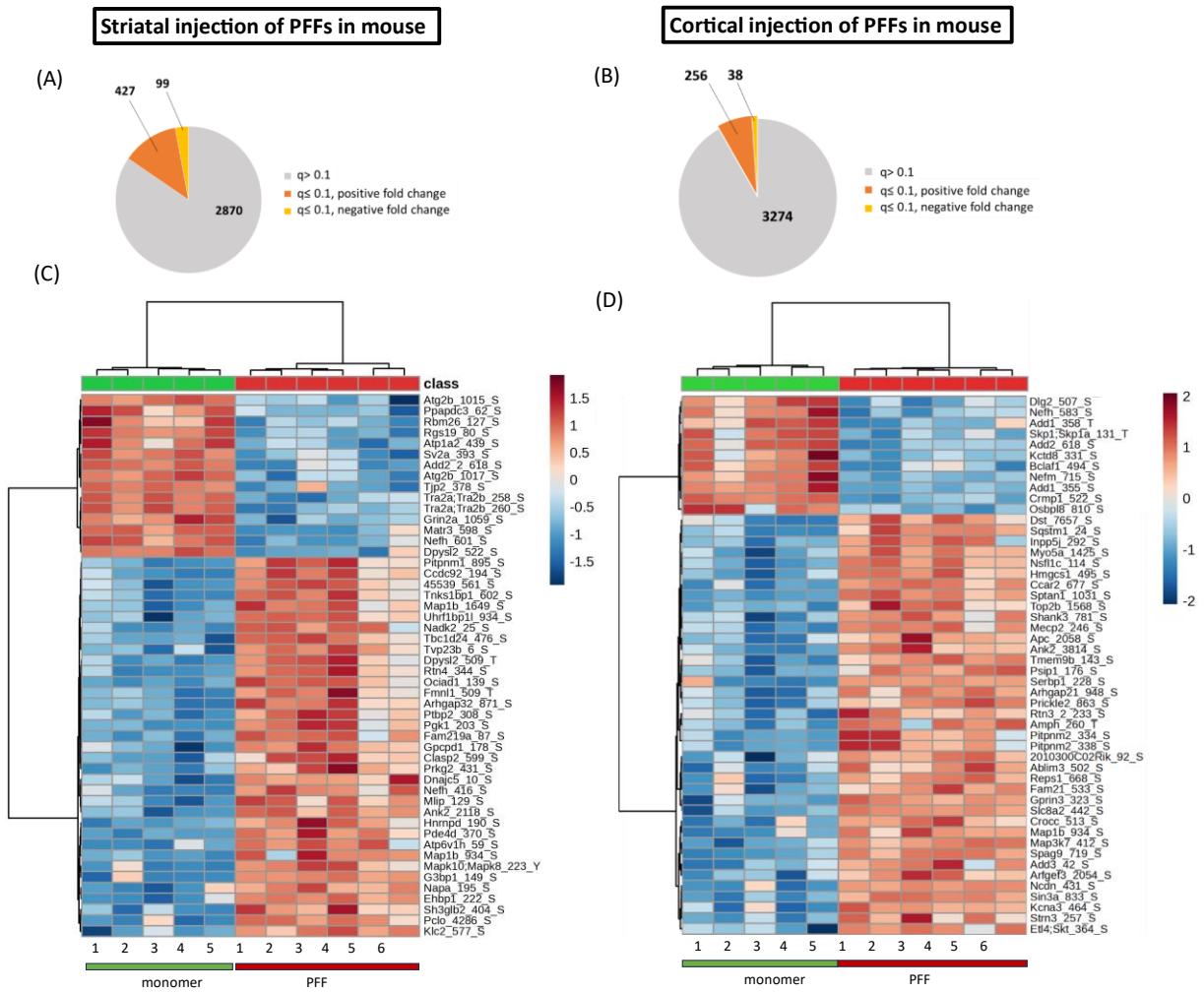

Supplementary figure 4: Extended analysis of phosphoproteomic changes in the sensorimotor cortex of mice following intrastriatal or intracortical injections of aSyn PFFs.

(A, B) Pie chart representations of phosphosite hits obtained via phosphoproteomic analysis of homogenates prepared from mouse sensorimotor cortex 3 months after injection with aSyn PFFs or monomer in the striatum (A) or cortex (B). Each chart shows the percentage of hits with q<0.1 with a positive or negative fold change (orange or yellow, respectively). Each hit was detected in ≥70% of samples in at least one experimental group.

(C, D) Cluster heatmaps showing log2-transformed intensities of the top 50 up- or down-regulated phosphosites (i.e., phosphosites with the lowest q-values) in the cortical homogenates described in (A) and (B), obtained from mice injected with aSyn PFFs or monomer in the striatum (C) or cortex (D). Red and blue correspond to an increase or decrease (respectively) in phosphosite levels in mice injected with PFFs versus monomer, and the color intensity represents the Z-score-normalized Log2(intensity) value. Peptide names are listed as 'protein name_phosphoresidue number.'

Supplementary Figure 5

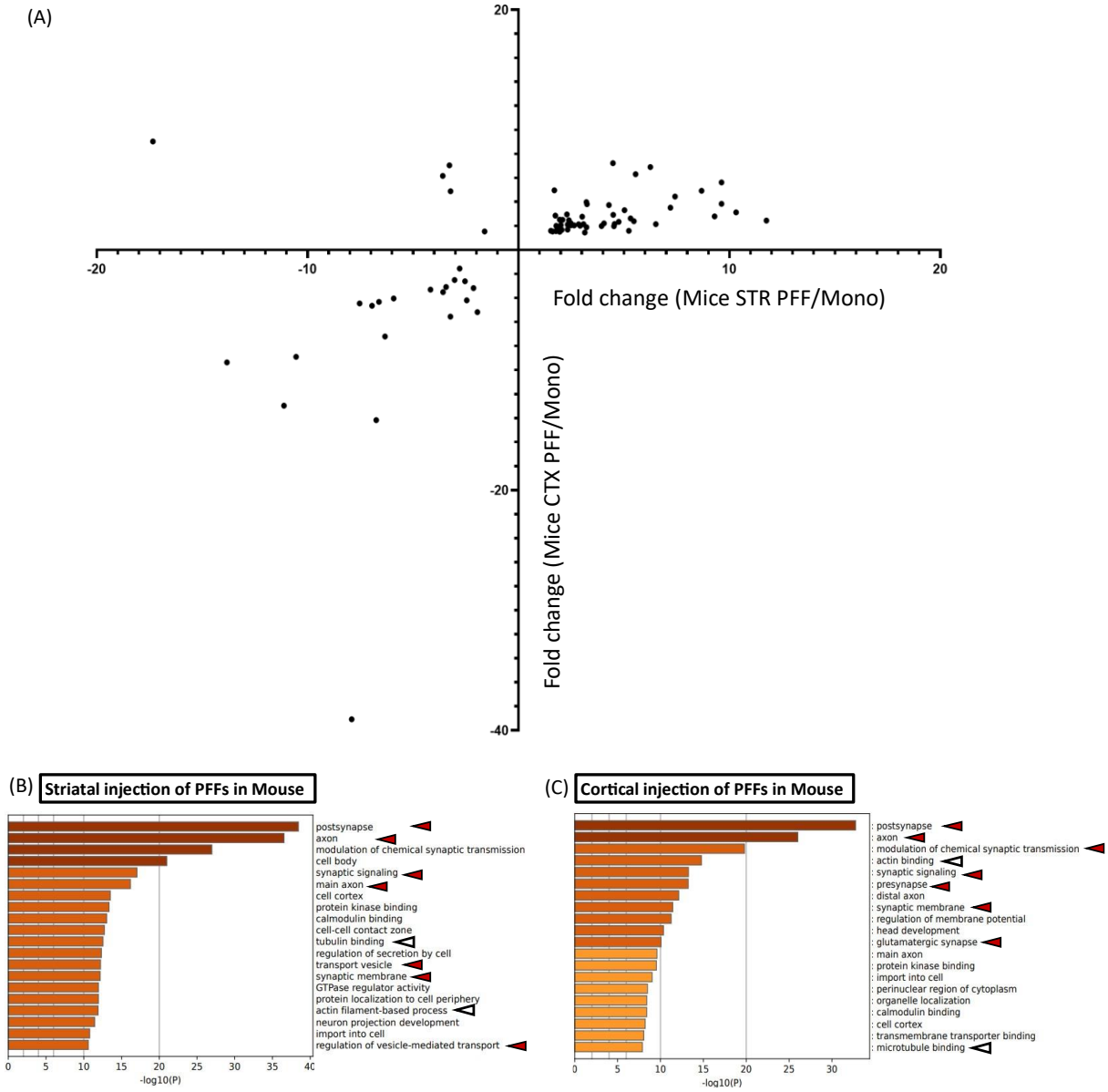

Supplementary Figure 5: Mice injected with aSyn PFFs in the striatum or cortex show evidence of altered synaptic function and cytoskeletal organization. (A). Fold changes of significantly altered phosphosites in cortex-injected versus striatum-injected mice. Charts showing enriched GO terms in the 'cellular localization' category that represent groups of phosphoproteins in mouse sensorimotor cortex impacted by PFF administration in the striatum, but not cortex (A), or in the cortex but not striatum (B), 3 months post-injection. GO analysis was carried out on proteins containing phosphosites with q<0.1 and a fold change of ≥2 (see Supporting Figure 4A, B). Arrowheads highlight items relevant to synaptic transmission (red) or the cytoskeleton (white).

Supplementary Figure 6

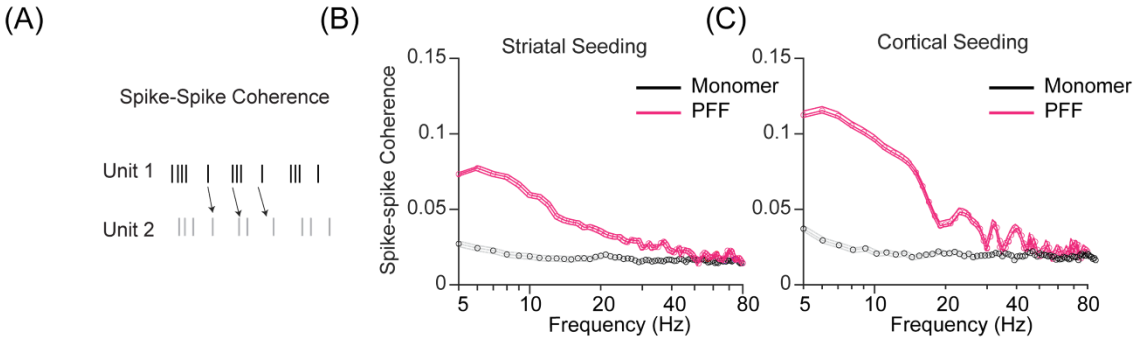

Supplementary Figure 6: Mice injected with aSyn PFFs in the striatum or cortex show evidence of altered network connectivity. (A) Schematic of spike-spike coherence where the coherence of two representative units is calculated based on fluctuations of spike rates (See methods). (B, C) Graphs showing frequency-resolved paired spike coherence data recorded in mouse sensorimotor cortex 3 months after injection with aSyn PFFs or monomer in the striatum (B) or cortex (C).

Supplementary Figure 7

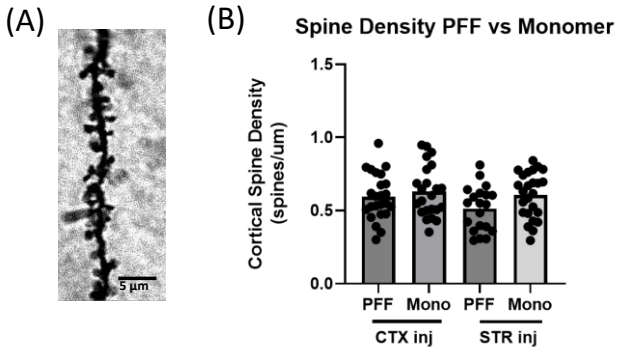

Supplementary Figure 7: Seeded aSyn aggregation does not lead to a change in cortical spine density in our mouse PFF model. (A) Representative image of a dendritic section from layer II/III of mouse sensorimotor cortex 3 months after intrastriatal aSyn PFF injection (scale bar: 5 µm). (B) Graph showing the spine density in sections prepared from mouse sensorimotor cortex 3 months after intrastriatal or intracortical injection with aSyn PFFs or monomer. Five dendritic sections were analyzed per mouse, and 4 to 5 mice were analyzed per group. A one-way ANOVA revealed no significant differences among any of the groups.

Acknowledgments

This work was supported by funds from the Parkinson's Foundation Visiting Scholar Award, Purdue Research Foundation, and The Bilsland Dissertation Fellowship (to S.D.); National Institute of General Medical Sciences (T32 GM007752) through the Graduate Training Program in Cellular and Molecular Pharmacology at UCSD (to L.M.R.) National Institutes of Health grants R01AG074273 and R01AG078185 (to X. C.); the Clinical and Translational Sciences Institute and Branfman Family Foundation (to J.C.R.);

Conflict of Interest

The authors declare no competing financial interests.

Author contributions:

S.D. and J.C.R conceived the study and prepared the manuscript with input from all authors; S.D. designed and coordinated all experiments, conducted most of the experiments including PFF preparation, *in vivo* surgeries, proteomics data analysis and visualization, immunohistochemistry, and imaging; J.H. assisted with in vivo experiments with rats; A.S. and T.J. assisted with in vivo experiments with mice and dendritic spine analysis; R.M. carried out proteomics sample processing and data acquisition, and assisted with proteomics analysis; L.M.R performed motif enrichment and kinase prediction analysis; H.F.K. performed in vivo recording experiments; C.R.F. carried out lipid profiling sample processing and data acquisition, and assisted with lipid profiling data analysis; J.F.M. assisted with proteomics sample preparation; X.C. supervised motif enrichment and kinase prediction analysis; K.J. supervised in vivo recording experiments; U.K.A. supervised proteomics sample processing and analysis; L.V.D. supervised PFF preparation and PD modeling in rodents, provided PFF for experiments in rat, and provided input on study design; J.C.R. supervised the study.

Data Availability

Raw proteomics data are available upon reasonable request from the corresponding author

References

1. Jellinger KA. Dementia with Lewy bodies and Parkinson's disease-dementia: current concepts and controversies. J Neural Transm (Vienna). 2018;125(4):615-50.
2. Russell A, Drozdova A, Wang W, Thomas M. The impact of dementia development concurrent with Parkinson's disease: a new perspective. CNS Neurol Disord Drug Targets. 2014;13(7):1160-8.
3. Shulman JM, De Jager PL, Feany MB. Parkinson's disease: genetics and pathogenesis. Annu Rev Pathol. 2011;6:193-222.
4. Crowther RA, Daniel SE, Goedert M. Characterisation of isolated alpha-synuclein filaments from substantia nigra of Parkinson's disease brain. Neurosci Lett. 2000;292(2):128-30.
5. Spillantini MG, Crowther RA, Jakes R, Hasegawa M, Goedert M. alpha-Synuclein in filamentous inclusions of Lewy bodies from Parkinson's disease and dementia with lewy bodies. Proc Natl Acad Sci U S A. 1998;95(11):6469-73.
6. Schweighauser M, Shi Y, Tarutani A, Kametani F, Murzin AG, Ghetti B, et al. Structures of alpha-synuclein filaments from multiple system atrophy. Nature. 2020;585(7825):464-9.
7. Pirooznia SK, Rosenthal LS, Dawson VL, Dawson TM. Parkinson Disease: Translating Insights from Molecular Mechanisms to Neuroprotection. Pharmacol Rev. 2021;73(4):33-97.
8. Braak H, Del Tredici K, Rub U, de Vos RA, Jansen Steur EN, Braak E. Staging of brain pathology related to sporadic Parkinson's disease. Neurobiol Aging. 2003;24(2):197-211.
9. Beach TG, Adler CH, Lue L, Sue LI, Bachalakuri J, Henry-Watson J, et al. Unified staging system for Lewy body disorders: correlation with nigrostriatal degeneration, cognitive impairment and motor dysfunction. Acta Neuropathol. 2009;117(6):613-34.
10. Paumier KL, Luk KC, Manfredsson FP, Kanaan NM, Lipton JW, Collier TJ, et al. Intrastriatal injection of pre-formed mouse alpha-synuclein fibrils into rats triggers alpha-synuclein pathology and bilateral nigrostriatal degeneration. Neurobiol Dis. 2015;82:185-99.
11. Henderson MX, Cornblath EJ, Darwich A, Zhang B, Brown H, Gathagan RJ, et al. Spread of alpha-synuclein pathology through the brain connectome is modulated by selective vulnerability and predicted by network analysis. Nat Neurosci. 2019;22(8):1248-57.
12. Luk KC, Kehm V, Carroll J, Zhang B, O'Brien P, Trojanowski JQ, et al. Pathological alpha-synuclein transmission initiates Parkinson-like neurodegeneration in nontransgenic mice. Science. 2012;338(6109):949-53.
13. Peng C, Trojanowski JQ, Lee VM. Protein transmission in neurodegenerative disease. Nat Rev Neurol. 2020;16(4):199-212.
14. Siderowf A, Concha-Marambio L, Lafontant DE, Farris CM, Ma Y, Urenia PA, et al. Assessment of heterogeneity among participants in the Parkinson's Progression Markers Initiative cohort using alpha-synuclein seed amplification: a cross-sectional study. Lancet Neurol. 2023;22(5):407-17.
15. Sharma M, Burre J. alpha-Synuclein in synaptic function and dysfunction. Trends Neurosci. 2023;46(2):153-66.
16. Runwal G, Edwards RH. The Membrane Interactions of Synuclein: Physiology and Pathology. Annu Rev Pathol. 2021;16:465-85.
17. Wang X, Becker K, Levine N, Zhang M, Lieberman AP, Moore DJ, et al. Pathogenic alpha-synuclein aggregates preferentially bind to mitochondria and affect cellular respiration. Acta Neuropathol Commun. 2019;7(1):41.
18. Zalon AJ, Quiriconi DJ, Pitcairn C, Mazzulli JR. alpha-Synuclein: Multiple pathogenic roles in trafficking and proteostasis pathways in Parkinson's disease. Neuroscientist. 2024:10738584241232963.
19. Flores-Leon M, Outeiro TF. More than meets the eye in Parkinson's disease and other synucleinopathies: from proteinopathy to lipidopathy. Acta Neuropathol. 2023;146(3):369-85.

20. Fanning S, Selkoe D, Dettmer U. Vesicle trafficking and lipid metabolism in synucleinopathy. Acta Neuropathol. 2021;141(4):491-510.
21. Volpicelli-Daley LA, Luk KC, Patel TP, Tanik SA, Riddle DM, Stieber A, et al. Exogenous alpha-synuclein fibrils induce Lewy body pathology leading to synaptic dysfunction and neuron death. Neuron. 2011;72(1):57-71.
22. Chen L, Nagaraja C, Daniels S, Fisk ZA, Dvorak R, Meyerdirk L, et al. Synaptic location is a determinant of the detrimental effects of alpha-synuclein pathology to glutamatergic transmission in the basolateral amygdala. Elife. 2022;11.
23. Froula JM, Henderson BW, Gonzalez JC, Vaden JH, McLean JW, Wu Y, et al. alpha-Synuclein fibril-induced paradoxical structural and functional defects in hippocampal neurons. Acta Neuropathol Commun. 2018;6(1):35.
24. Calabresi P, Di Lazzaro G, Marino G, Campanelli F, Ghiglieri V. Advances in understanding the function of alpha-synuclein: implications for Parkinson's disease. Brain. 2023;146(9):3587-97.
25. Calabresi P, Mechelli A, Natale G, Volpicelli-Daley L, Di Lazzaro G, Ghiglieri V. Alpha-synuclein in Parkinson's disease and other synucleinopathies: from overt neurodegeneration back to early synaptic dysfunction. Cell Death Dis. 2023;14(3):176.
26. Garcia-Yague AJ, Lastres-Becker I, Stefanis L, Vassilatis DK, Cuadrado A. alpha-Synuclein Induces the GSK-3-Mediated Phosphorylation and Degradation of NURR1 and Loss of Dopaminergic Hallmarks. Mol Neurobiol. 2021;58(12):6697-711.
27. Ryu MY, Kim DW, Arima K, Mouradian MM, Kim SU, Lee G. Localization of CKII beta subunits in Lewy bodies of Parkinson's disease. J Neurol Sci. 2008;266(1-2):9-12.
28. Li J, Wilkinson B, Clementel VA, Hou J, O'Dell TJ, Coba MP. Long-term potentiation modulates synaptic phosphorylation networks and reshapes the structure of the postsynaptic interactome. Sci Signal. 2016;9(440):rs8.
29. Engholm-Keller K, Waardenberg AJ, Muller JA, Wark JR, Fernando RN, Arthur JW, et al. The temporal profile of activity-dependent presynaptic phospho-signalling reveals long-lasting patterns of poststimulus regulation. PLoS Biol. 2019;17(3):e3000170.
30. Kohansal-Nodehi M, Chua JJ, Urlaub H, Jahn R, Czernik D. Analysis of protein phosphorylation in nerve terminal reveals extensive changes in active zone proteins upon exocytosis. Elife. 2016;5.
31. Battis K, Xiang W, Winkler J. The Bidirectional Interplay of alpha-Synuclein with Lipids in the Central Nervous System and Its Implications for the Pathogenesis of Parkinson's Disease. Int J Mol Sci. 2023;24(17).
32. Dent EW, Merriam EB, Hu X. The dynamic cytoskeleton: backbone of dendritic spine plasticity. Curr Opin Neurobiol. 2011;21(1):175-81.
33. Blumenstock S, Rodrigues EF, Peters F, Blazquez-Llorca L, Schmidt F, Giese A, et al. Seeding and transgenic overexpression of alpha-synuclein triggers dendritic spine pathology in the neocortex. EMBO Mol Med. 2017;9(5):716-31.
34. Burre J. The Synaptic Function of alpha-Synuclein. J Parkinsons Dis. 2015;5(4):699-713.
35. Bopp R, Holler-Rickauer S, Martin KA, Schuhknecht GF. An Ultrastructural Study of the Thalamic Input to Layer 4 of Primary Motor and Primary Somatosensory Cortex in the Mouse. J Neurosci. 2017;37(9):2435-48.
36. Stoyka LE, Arrant AE, Thrasher DR, Russell DL, Freire J, Mahoney CL, et al. Behavioral defects associated with amygdala and cortical dysfunction in mice with seeded alpha-synuclein inclusions. Neurobiol Dis. 2020;134:104708.
37. Goralski TM, Meyerdirk L, Breton L, Brasseur L, Kurgat K, DeWeerd D, et al. Spatial transcriptomics reveals molecular dysfunction associated with cortical Lewy pathology. Nat Commun. 2024;15(1):2642.
38. Harding AJ, Halliday GM. Cortical Lewy body pathology in the diagnosis of dementia. Acta Neuropathol. 2001;102(4):355-63.

39. Patterson JR, Duffy MF, Kemp CJ, Howe JW, Collier TJ, Stoll AC, et al. Time course and magnitude of alpha-synuclein inclusion formation and nigrostriatal degeneration in the rat model of synucleinopathy triggered by intrastriatal alpha-synuclein preformed fibrils. Neurobiol Dis. 2019;130:104525.
40. Schulz-Schaeffer WJ. The synaptic pathology of alpha-synuclein aggregation in dementia with Lewy bodies, Parkinson's disease and Parkinson's disease dementia. Acta Neuropathol. 2010;120(2):131-43.
41. Ma SX, Seo BA, Kim D, Xiong Y, Kwon SH, Brahmachari S, et al. Complement and Coagulation Cascades are Potentially Involved in Dopaminergic Neurodegeneration in alpha-Synuclein-Based Mouse Models of Parkinson's Disease. J Proteome Res. 2021;20(7):3428-43.
42. Penkov S, Fedorova M. Membrane Epilipidome-Lipid Modifications, Their Dynamics, and Functional Significance. Cold Spring Harb Perspect Biol. 2024;16(7).
43. Bridi JC, Hirth F. Mechanisms of alpha-Synuclein Induced Synaptopathy in Parkinson's Disease. Front Neurosci. 2018;12:80.
44. Patterson JR, Kochmanski J, Stoll AC, Kubik M, Kemp CJ, Duffy MF, et al. Transcriptomic profiling of early synucleinopathy in rats induced with preformed fibrils. NPJ Parkinsons Dis. 2024;10(1):7.
45. Tasaki S, Xu J, Avey DR, Johnson L, Petyuk VA, Dawe RJ, et al. Inferring protein expression changes from mRNA in Alzheimer's dementia using deep neural networks. Nat Commun. 2022;13(1):655.
46. Mangleburg CG, Wu T, Yalamanchili HK, Guo C, Hsieh YC, Duong DM, et al. Integrated analysis of the aging brain transcriptome and proteome in tauopathy. Mol Neurodegener. 2020;15(1):56.
47. Parra-Rivas LA, Madhivanan K, Aulston BD, Wang L, Prakashchand DD, Boyer NP, et al. Serine-129 phosphorylation of alpha-synuclein is an activity-dependent trigger for physiologic protein-protein interactions and synaptic function. Neuron. 2023;111(24):4006-23 e10.
48. Ramalingam N, Jin SX, Moors TE, Fonseca-Ornelas L, Shimanaka K, Lei S, et al. Dynamic physiological alpha-synuclein S129 phosphorylation is driven by neuronal activity. NPJ Parkinsons Dis. 2023;9(1):4.
49. Ferrer I, Andres-Benito P, Ausin K, Pamplona R, Del Rio JA, Fernandez-Irigoyen J, et al. Dysregulated protein phosphorylation: A determining condition in the continuum of brain aging and Alzheimer's disease. Brain Pathol. 2021;31(6):e12996.
50. Fujita K, Homma H, Kondo K, Ikuno M, Yamakado H, Tagawa K, et al. Ser46-Phosphorylated MARCKS Is a Marker of Neurite Degeneration at the Pre-aggregation Stage in PD/DLB Pathology. eNeuro. 2018;5(4).
51. Killinger BA, Marshall LL, Chatterjee D, Chu Y, Bras J, Guerreiro R, et al. In situ proximity labeling identifies Lewy pathology molecular interactions in the human brain. Proc Natl Acad Sci U S A. 2022;119(5).
52. Okochi M, Walter J, Koyama A, Nakajo S, Baba M, Iwatsubo T, et al. Constitutive phosphorylation of the Parkinson's disease associated alpha-synuclein. J Biol Chem. 2000;275(1):390-7.
53. Borgo C, D'Amore C, Sarno S, Salvi M, Ruzzene M. Protein kinase CK2: a potential therapeutic target for diverse human diseases. Signal Transduct Target Ther. 2021;6(1):183.
54. Zhang C, Vilk G, Canton DA, Litchfield DW. Phosphorylation regulates the stability of the regulatory CK2beta subunit. Oncogene. 2002;21(23):3754-64.
55. Litchfield DW, Lozeman FJ, Cicirelli MF, Harrylock M, Ericsson LH, Piening CJ, et al. Phosphorylation of the beta subunit of casein kinase II in human A431 cells. Identification of the autophosphorylation site and a site phosphorylated by p34cdc2. J Biol Chem. 1991;266(30):20380-9.
56. Rosenberger AF, Morrema TH, Gerritsen WH, van Haastert ES, Snkhchyan H, Hilhorst R, et al. Increased occurrence of protein kinase CK2 in astrocytes in Alzheimer's disease pathology. J Neuroinflammation. 2016;13:4.
57. Zhang H, Griggs A, Rochet JC, Stanciu LA. In vitro study of alpha-synuclein protofibrils by cryo-EM suggests a Cu(2+)-dependent aggregation pathway. Biophys J. 2013;104(12):2706-13.

58. Volpicelli-Daley LA, Luk KC, Lee VM. Addition of exogenous alpha-synuclein preformed fibrils to primary neuronal cultures to seed recruitment of endogenous alpha-synuclein to Lewy body and Lewy neurite-like aggregates. Nat Protoc. 2014;9(9):2135-46.
59. Sanyal A, Dutta S, Camara A, Chandran A, Koller A, Watson BG, et al. Alpha-Synuclein Is a Target of Fic-Mediated Adenylylation/AMPylation: Possible Implications for Parkinson's Disease. J Mol Biol. 2019;431(12):2266-82.
60. Bligh EG, Dyer WJ. A rapid method of total lipid extraction and purification. Can J Biochem Physiol. 1959;37(8):911-7.
61. Khan HF, Dutta S, Scott AN, Xiao S, Yadav S, Chen X, et al. Site-specific seeding of Lewy pathology induces distinct pre-motor cellular and dendritic vulnerabilities in the cortex. Nat Commun. 2024;15(1):10775.
62. Glatter T, Ludwig C, Ahrne E, Aebersold R, Heck AJ, Schmidt A. Large-scale quantitative assessment of different in-solution protein digestion protocols reveals superior cleavage efficiency of tandem Lys-C/trypsin proteolysis over trypsin digestion. J Proteome Res. 2012;11(11):5145-56.
63. Zembroski AS, Buhman KK, Aryal UK. Proteome and phosphoproteome characterization of liver in the postprandial state from diet-induced obese and lean mice. J Proteomics. 2021;232:104072.
64. Xie Z, Ferreira CR, Virequ AA, Cooks RG. Multiple reaction monitoring profiling (MRM profiling): Small molecule exploratory analysis guided by chemical functionality. Chem Phys Lipids. 2021;235:105048.
65. Reis LG, Casey TM, Sobreira TJP, Cooper BR, Ferreira CR. Step-by-Step Approach to Build Multiple Reaction Monitoring (MRM) Profiling Instrument Acquisition Methods for Class-based Lipid Exploratory Analysis by Mass Spectrometry. J Biomol Tech. 2023;34(2).
66. Tyanova S, Temu T, Cox J. The MaxQuant computational platform for mass spectrometry-based shotgun proteomics. Nat Protoc. 2016;11(12):2301-19.
67. Tyanova S, Temu T, Sinitcyn P, Carlson A, Hein MY, Geiger T, et al. The Perseus computational platform for comprehensive analysis of (prote)omics data. Nat Methods. 2016;13(9):731-40.
68. UniProt C. UniProt: the universal protein knowledgebase in 2021. Nucleic Acids Res. 2021;49(D1):D480-D9.
69. Mohallem R, Aryal UK. Nuclear Phosphoproteome Reveals Prolyl Isomerase PIN1 as a Modulator of Oncogene-Induced Senescence. Mol Cell Proteomics. 2024;23(2):100715.
70. Zhou Y, Zhou B, Pache L, Chang M, Khodabakhshi AH, Tanaseichuk O, et al. Metascape provides a biologist-oriented resource for the analysis of systems-level datasets. Nat Commun. 2019;10(1):1523.
71. Pang Z, Chong J, Zhou G, de Lima Morais DA, Chang L, Barrette M, et al. MetaboAnalyst 5.0: narrowing the gap between raw spectra and functional insights. Nucleic Acids Res. 2021;49(W1):W388-W96.
72. Berkers CR, van Leeuwen FW, Groothuis TA, Peperzak V, van Tilburg EW, Borst J, et al. Profiling proteasome activity in tissue with fluorescent probes. Mol Pharm. 2007;4(5):739-48.
73. Ysselstein D, Joshi M, Mishra V, Griggs AM, Asiago JM, McCabe GP, et al. Effects of impaired membrane interactions on alpha-synuclein aggregation and neurotoxicity. Neurobiol Dis. 2015;79:150-63.
74. Mitra PP, Pesaran B. Analysis of dynamic brain imaging data. Biophys J. 1999;76(2):691-708.
75. Jarvis MR, Mitra PP. Sampling properties of the spectrum and coherency of sequences of action potentials. Neural Comput. 2001;13(4):717-49.
76. Pesaran B, Pezaris JS, Sahani M, Mitra PP, Andersen RA. Temporal structure in neuronal activity during working memory in macaque parietal cortex. Nat Neurosci. 2002;5(8):805-11.
77. Mitchell CJ, De Houwer J, Lovibond PF. The propositional nature of human associative learning. Behav Brain Sci. 2009;32(2):183-98; discussion 98-246.
78. Crooks GE, Hon G, Chandonia JM, Brenner SE. WebLogo: a sequence logo generator. Genome Res. 2004;14(6):1188-90.

79. Chou MF, Schwartz D. Biological sequence motif discovery using motif-x. Curr Protoc Bioinformatics. 2011;Chapter 13:13 5 1- 5 24.
80. Wozniak JM, Gonzalez DJ. PTMphinder: an R package for PTM site localization and motif extraction from proteomic datasets. PeerJ. 2019;7:e7046.
81. Blom N, Sicheritz-Ponten T, Gupta R, Gammeltoft S, Brunak S. Prediction of post-translational glycosylation and phosphorylation of proteins from the amino acid sequence. Proteomics. 2004;4(6):1633-49.